Athena MIMOS II Mössbauer spectrometer investigation

G. Klingelhöfer,[1] R. V. Morris,[2] B. Bernhardt,[1] D. Rodionov,[1,3] P. A. de Souza Jr.,[1,4]
S. W. Squyres,[5] J. Foh,[1] E. Kankeleit,[6] U. Bonnes,[6] R. Gellert,[1] C. Schröder,[1] S. Linkin,[3]
E. Evlanov,[3] B. Zubkov,[3] and O. Prilutski[3]

[1]   Mössbauer spectroscopy is a powerful tool for quantitative mineralogical analysis of Fe-bearing materials. The miniature Mössbauer spectrometer MIMOS II is a component of the Athena science payload launched to Mars in 2003 on both Mars Exploration Rover missions. The instrument has two major components: (1) a rover-based electronics board that contains power supplies, a dedicated central processing unit, memory, and associated support electronics and (2) a sensor head that is mounted at the end of the instrument deployment device (IDD) for placement of the instrument in physical contact with soil and rock. The velocity transducer operates at a nominal frequency of $\sim$25 Hz and is equipped with two ^{57}Co/Rh Mössbauer sources. The reference source ($\sim$5 mCi landed intensity), reference target (α-Fe$_2$O$_3$ plus α-Fe^0), and PIN-diode detector are configured in transmission geometry and are internal to the instrument and used for its calibration. The analysis Mössbauer source ($\sim$150 mCi landed intensity) irradiates Martian surface materials with a beam diameter of $\sim$1.4 cm. The backscatter radiation is measured by four PIN-diode detectors. Physical contact with surface materials is sensed with a switch-activated contact plate. The contact plate and reference target are instrumented with temperature sensors. Assuming $\sim$18% Fe for Martian surface materials, experiment time is 6–12 hours during the night for quality spectra (i.e., good counting statistics); 1–2 hours is sufficient to identify and quantify the most abundant Fe-bearing phases. Data stored internal to the instrument for selectable return to Earth include Mössbauer and pulse-height analysis spectra (512 and 256 channels, respectively) for each of the five detectors in up to 13 temperature intervals (65 Mössbauer spectra), engineering data for the velocity transducer, and temperature measurements. The total data volume is $\sim$150 kB. The mass and power consumption are $\sim$500 g ($\sim$400 g for the sensor head) and $\sim$2 W, respectively. The scientific measurement objectives of the Mössbauer investigation are to obtain for rock, soil, and dust (1) the mineralogical identification of iron-bearing phases (e.g., oxides, silicates, sulfides, sulfates, and carbonates), (2) the quantitative measurement of the distribution of iron among these iron-bearing phases (e.g., the relative proportions of iron in olivine, pyroxenes, ilmenite, and magnetite in a basalt), (3) the quantitative measurement of the distribution of iron among its oxidation states (e.g., Fe^{2+}, Fe^{3+}, and Fe^{6+}), and (4) the characterization of the size distribution of magnetic particles. Special geologic targets of the Mössbauer investigation are dust collected by the Athena magnets and interior rock and soil surfaces exposed by the Athena Rock Abrasion Tool and by trenching with rover wheels.   *INDEX TERMS:* 5415 Planetology: Solid Surface Planets: Erosion and weathering; 5470 Planetology: Solid Surface Planets: Surface materials and properties; 6225 Planetology: Solar System Objects: Mars; 3929 Mineral Physics: NMR, Mossbauer spectroscopy, and other magnetic techniques; 3672 Mineralogy and Petrology: Planetary mineralogy and petrology (5410); *KEYWORDS:* Mössbauer spectroscopy, iron mineralogy, Mars, weathering, instrumentation, MIMOS II

[1]Institute for Inorganic and Analytical Chemistry, Johannes Gutenberg University, Mainz, Germany.

[2]NASA Johnson Space Center, Houston, Texas, USA.

[3]Space Research Institute IKI, Moscow, Russia.

[4]Pelletizing Department, Companhia Vale do Rio Doce, Vitoria, Brazil.

[5]Department of Astronomy, Cornell University, Ithaca, New York, USA.

[6]Nuclear Physics Institute, Darmstadt University of Technology, Darmstadt, Germany.

1. Introduction

[2] Iron Mössbauer spectroscopy (FeMS) has been used in Earth-based laboratories to study the mineralogical composition of iron-bearing phases in a variety of planetary samples, including lunar samples returned to Earth by American Apollo astronauts and Soviet robotic missions and meteorites that have asteroidal and Martian origins [e.g., *Fernandez-Moran et al.*, 1970; *Gay et al.*, 1970; *Herzenberg and Riley*, 1970; *Herzenberg et al.*, 1971; *Housley et al.*, 1970, 1971, 1973; *Huffman et al.*, 1974; *Wdowiak and Agresti*, 1984; *Madsen et al.*, 1986; *Vieira et al.*, 1986; *Solberg and Burns*, 1989; *Burns and Martinez*, 1991; *Burns*, 1993; *Morris et al.*, 1998a; *Graff et al.*, 2003]. A variety of terrestrial samples that are analogues of Martian surface regions have also been studied by FeMS [e.g., *Morris et al.*, 1989, 1990, 1993, 1995, 1996, 1997, 1998b, 2000, 2001a; *Burns and Fisher*, 1990; *Straub et al.*, 1991; *Bell et al.*, 1993; *Fegley et al.*, 1995; *Golden et al.*, 1993; *Bishop et al.*, 1993, 1995; *Bishop and Murad*, 1996; *Klingelhöfer et al.*, 1996; *Wade et al.*, 1999; *Lane et al.*, 2002]. To date, no in situ FeMS measurements have been made as part of any planetary mission. With the launch in 2003 of MIMOS II Mössbauer spectrometers aboard the European Space Agency (ESA) Beagle-2 mission and the two NASA Mars Exploration Rover (MER) missions, this situation will change.

[3] The scientific basis for landing a Mössbauer spectrometer on Mars is extensively discussed by Knudsen [*Knudsen*, 1989; *Knudsen et al.*, 1990, 1992]. The scientific objectives of the MIMOS II Mössbauer spectrometer investigation are (1) to identify the mineralogical composition and (2) to measure the relative abundance of iron-bearing phases (e.g., silicates, oxides, carbonates, phyllosilicates, hydroxides, phosphates, sulfides, and sulfates), (3) to measure the distribution of Fe among its oxidation states (e.g., Fe^{2+}, Fe^{3+}, and Fe^{6+}), and (4) to distinguish between magnetically ordered and paramagnetic phases and provide, from measurements at different temperatures, characterization of the size distribution of magnetic particles. Magnetic particles collected by the Athena magnets and internal rock surfaces exposed by the Rock Abrasion Tool (RAT) are special targets for the MER MIMOS II instruments. The FeMS data characterize the present state of Martian surface materials and provide constraints on climate history and weathering processes by which the surface evolved to its present state. FeMS can identify primary igneous minerals such as iron-bearing olivine and pyroxene and weathering products which do (e.g., goethite and jarosite) and do not (e.g., hematite and maghemite) contain volatiles as a part of their structures. Iron-bearing sulfides (e.g., pyrite and pyrrhotite) and carbonates (e.g., siderite) can also be detected.

[4] By determining the size distribution of iron oxide particles, Mössbauer analyses can differentiate between, for example, low-temperature (e.g., nanophase ferric oxide particles formed during palagonitization [e.g., *Morris et al.*, 2000, 2001a]) and hydrothermal (e.g., hematite particle formation during associated with an impact event into a water-rich target [e.g., *Morris et al.*, 1996]) alteration

processes. Another question is whether the Martian meteorites can be related to actual materials on the Martian surface. Mössbauer spectroscopy can directly address this question through comparison of laboratory Mössbauer spectra for Martian meteorites and in situ spectra for the Martian surface.

[5] This paper is divided into five main sections. In section 2, we briefly discuss the principles of Mössbauer spectroscopy. In section 3, we give a technical description the MIMOS II Mössbauer spectrometers that were fabricated for the two MER rovers and the Mars-Express Beagle-2 lander. MIMOS II performance validation on geologic samples is discussed in section 4. In section 5, we develop operational considerations, including analysis of Mössbauer spectra returned from Mars.

2. Principles and Practice of Mössbauer Spectroscopy

2.1. Mössbauer Effect for ^{57}Fe

[6] The Mössbauer effect, the recoilless emission and resonant absorption of γ-rays by certain nuclei in solid materials (in our application, ^{57}Fe), has been extensively reviewed in the literature [e.g., *Wertheim*, 1964; *Wegener*, 1966; *Greenwood and Gibb*, 1971; *Bancroft*, 1973; *Hawthorne*, 1988; *Burns and Solberg*, 1990; *Burns*, 1993]. We give a brief overview here from the perspective of application to Martian surface materials.

[7] Resonant emission and absorption of γ-rays means that absorbed and emitted γ-rays have approximately the same energy. The requirement for this to occur with non-zero probability is that the emitting and absorbing nuclei must be in solid lattices having sufficient mass so that there is negligible nuclear recoil energy (i.e., "recoil-free" nuclear transitions). Because kinetic energy (=$p^2/2m$, where p and m are momentum of the absorbed or emitted photon and mass of the absorbing or emitting body, respectively) is inversely proportional to mass at constant momentum, the recoil energy is virtually zero when the mass of the solid lattice is $\sim10^{18}$ times the nuclear mass, i.e., a small particle weighing ~0.1 mg. Even in a solid, however, the emission (or absorption) of the γ-rays can involve energy transfer to lattice vibrations (phonons) in the crystal so that the Mössbauer effect is not observed. The probability of emissions that take place without inducing any phonons is named, as in X-ray diffraction, the Debye-Waller factor f. In general, this factor depends on temperature, the Debye temperature of the crystal, and the γ-ray energy [*Gonser*, 1986]. The probability of recoil-free emission or absorption is 0.76 for ^{57}Fe in α-iron metal (α-Fe^0) at room temperature [*Gonser*, 1986]. Normally, ^{57}Co is used as the emission source for Fe Mössbauer spectroscopy. ^{57}Co decays by electron capture to the second excited state of ^{57}Fe at 136.4 keV ($\sim99.8\%$ probability) which subsequently undergoes decay to its first excited state at 122.0 keV ($\sim91\%$ probability) and ground state ($\sim9\%$ probability). The first excited state undergoes recoil-free decay to the ground state by emission of the 14.4 keV Mössbauer γ-ray (10%

probability), internal conversion electrons (~90% probability), and X-rays (at ~6.4 keV).

[8] The energies of γ-rays from recoilless emissions are very precise (14.401 keV for ^{57}Fe), and their energy distribution has ideally a Lorentzian line shape with a width of ~4.7 neV that approaches the theoretical width imposed by the Heisenberg uncertainty principle. This width is in general less than the difference in energy between nuclear energy levels that result from different nuclear environments caused by, for example, different oxidation states and/or mineralogical environments. Therefore recoil-free emission of 14.4 keV γ-rays by ^{57}Fe in one lattice will not undergo recoilless absorption in another lattice if the nuclear environments are too different, unless the energy of the emitted γ-ray or the energy of the nuclear energy levels in the absorber is changed slightly. Usually, the energy of emitted recoilless γ-rays is changed by exploiting the Doppler effect, i.e., by moving the source. For ^{57}Fe, energy "scanning" through limits of ±10 mm/s is sufficient; positive velocities refer to motion of the source toward the absorber. The Mössbauer spectrum is then counts passing through (or emitted by) an absorbing sample as a function of the relative velocity of the source and sample.

[9] The nuclear energy levels of ^{57}Fe (ground and first excited states with nuclear spins of 1/2 and 3/2, respectively) can be changed (i.e., shifted or split) by electric and/or magnetic fields acting at the nucleus. The electrical quadrupole interaction leads to both the isomer shift (IS) and the electric quadrupole splitting/shift (QS). The nuclear Zeeman hyperfine interaction leads to the internal magnetic field (B_{hf}) [Wegener, 1966]. The hyperfine interactions can be translated into three parameters that are measured from Mössbauer spectra by curve fitting, and it is these parameters that characterize the oxidation state and mineralogical environment of the ^{57}Fe nucleus, which has ~2.2% natural abundance. We discuss these derived parameters next. The energy level diagrams are shown schematically in Figure 1.

2.1.1. Isomer Shift (IS, mm/s)

[10] The isomer shift (or "center shift") results from the interaction of the nuclear charge distribution with the electron density at the nucleus, which occurs primarily from s electrons, because they have non-zero probability of being located at the nucleus. The ^{57}Co source is normally imbedded in a matrix that has high symmetry and no magnetic order (e.g., Rh metal) so that monochromatic γ-rays are emitted (because the ^{57}Fe nuclear states are not split). If nuclear energy levels of ^{57}Fe in the absorber are also not split, a singlet is obtained, and the difference in energy (velocity) between the source and absorber is the isomer shift (Figure 1). When splitting is present, the isomer shift is referenced to the midpoint (center) of the doublet or sextet spectrum (Figure 1). The usual practice is to report values of IS relative to the midpoint of the Mössbauer spectrum for α-Fe^0.

2.1.2. Quadrupole Splitting (QS, mm/s)

[11] When the site symmetry at the ^{57}Fe nucleus is below cubic, an electric field gradient may be present there. This gradient interacts with the nuclear quadrupole moment and splits the energy level of the excited state into two states (in the simplest case, ±1/2 and ±3/2), so that two transitions (a doublet) are possible (Figure 1). The magnitude of the quadrupole splitting is the absolute value of the difference in velocity of the two lines of the doublet (QS = $|v_2 - v_1|$),
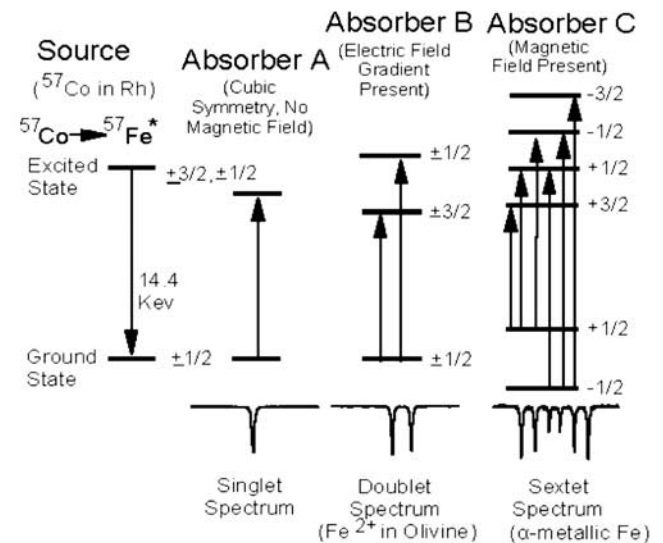

Figure 1. Energy level diagram for ^{57}Fe showing singlet emission of 14.4 keV γ-rays from the Mössbauer source and absorption of the γ-rays in three different nuclear environments.

or twice the value of the shift (up or down) induced by electric quadrupole interaction (Figure 1). When the angle between the direction of propagation of the incident γ-rays and the direction of the principal axis of the electric field gradient is randomly distributed (as in a polycrystalline sample), the doublet lines generally have equal intensity. For a single crystal, the intensity ratios are 3:1 and 5:3 when the angle equals 0° and 90°, respectively.

2.1.3. Internal Magnetic Field (B_{hf}, T)

[12] When a magnetic field is present at the nucleus, all of the nuclear energy levels are split (nuclear Zeeman effect), and six transitions are possible under the constraint of spin allowed transitions (nuclear spin changes of 0 and ±1 as in Figure 1). The magnetic field can be an intrinsic property of the material or can imposed by an external magnet. When there is no electric field gradient present (QS = 0), the six lines are symmetrically placed about the midpoint of the spectrum. This is the case for α-Fe^0. The magnitude of the internal field (in T) can be calculated from the velocity positions (mm/s) of the both lines at highest and lowest velocities (v_6 and v_1, respectively) from the equation, $B_{hf} = 3.108 \times (v_6 - v_1)$.

[13] The situation when both an electric field gradient and an internal magnetic field are present can be very complicated. Fortunately, in most cases the magnetic interaction is much stronger, and the electrical interaction can be treated as a perturbation. In this case, QS can be calculated from the formula QS = $1/2[(v_6 - v_5) - (v_2 - v_1)]$, where the numbers refer to the lines of the sextet numbered from lowest to highest velocity. B_{hf} is calculated as described above. As in the case of the doublet spectrum, QS is twice the quadrupole shift (up or down) experienced by any one of the nuclear hyperfine levels.

[14] The relative intensities of the lines in the sextet depend on the angle between the propagation direction of
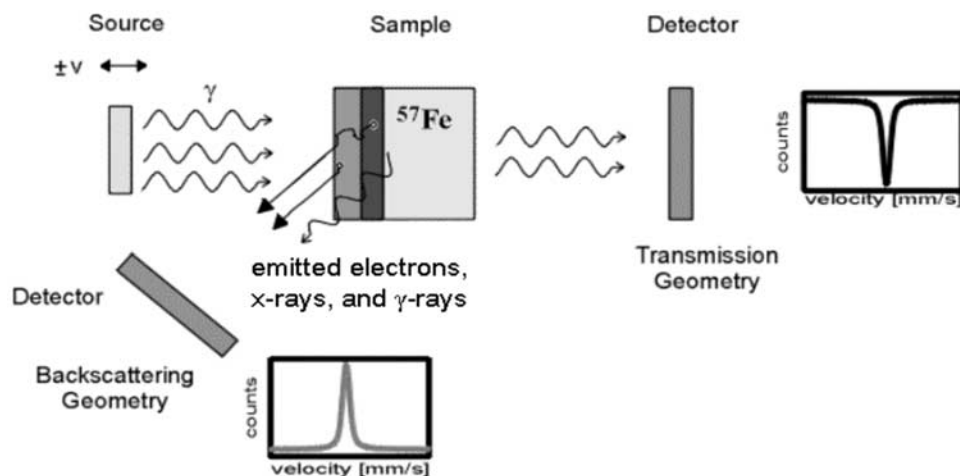
Figure 2. Schematic illustration of the measurement geometry for Mössbauer spectrometers. In transmission geometry, the absorber (sample) is between the nuclear source of 14.4 keV γ-rays (normally [57]Co/Rh) and the detector. The peaks are negative features, and the absorber should be "thin" with respect to absorption of the γ-rays to minimize non-linear effects. In emission (backscatter) Mössbauer spectroscopy, the radiation source and detector are on the same side of the sample. The peaks are positive features, corresponding to recoilless emission of 14.4 keV γ-rays and conversion X-rays and electrons. For both measurement geometries, Mössbauer spectra are counts per channel as a function of the Doppler velocity (normally in units of mm/s relative to the midpoint of the spectrum of α-Fe[0]). See color version of this figure in the HTML.

the incident γ-rays and the direction of magnetization. When the directions are randomly distributed (isotropic) as is often the case for a powder, the intensity ratios are 3:2:1:1:2:3. When the angle is 90°, the intensity ratio is 3:4:1:1:4:3. When the angle is 0°, the intensity ratio is 3:0:1:1:0:3; i.e., lines 2 and 5 are not present.

2.2. Basic Mössbauer Instrument Design

[15] Standard laboratory Mössbauer spectrometers have a velocity transducer, waveform generator and synchronizer, multichannel analyzer, γ-ray detection system, a velocity calibration device, a radiation source (normally [57]Co in a Rh metal matrix for [57]Fe Mössbauer spectroscopy), computer, and optionally a cryostat or oven for temperature-dependent measurements and a magnet for imposing an external field on the sample. In transmission measurement geometry (Figure 2), the absorber (sample) is between the source and detector, so that negative peaks are observed corresponding to absorption of 14.4 keV γ-rays. In backscatter (or emission) measurement geometry, the source and detector are on the same side of the emitter (sample), so that positive peaks are observed corresponding to emission of 14.4 keV γ-rays.

[16] Mössbauer spectra are generated by the velocity-sweep method in which the velocity transducer moves the source (or sample) repeatedly over a range of velocities, while simultaneously γ-rays transmitted through (or emitted by) the sample are counted into synchronized channels. In most instruments, the source is mounted on the vibration axis of an electromagnetic transducer (loudspeaker system) which is moved according to a voltage waveform applied to the driving coil of the system. Typically, the transducer is operated at constant acceleration with a triangular waveform at a frequency of 5−50 Hz. Detector counts are stored in a memory (typically 1024 channels). Synchronization of the channel number in the memory and the instantaneous

velocity of the source is achieved by advancing the memory address one by one. This is done through an external clock which subdivides the period of the waveform applied to the drive system into the number of available channels. The triangular waveform and 1024 memory channels produces two mirror-imaged Mössbauer spectra each with 512 channels. With sufficiently good velocity linearity, the two spectra can be easily combined (to increase the signal-to-noise ratio) to give one 512 channel Mössbauer spectrum.

2.3. Basics of Mössbauer Data Analysis

[17] In the simplest case for transmission measurements on an ideal absorber, Mössbauer spectra are the superposition of one or more spectral patterns (singlets, doublets, or sextets, as in Figure 1) whose individual peaks have Lorentzian line shape. The area of each spectral pattern is proportional to the number of absorbing nuclei times the recoilless fraction f. An ideal absorber has ∼10 mg/cm^{2} of natural Fe and is uniform. Uniformity is achieved by using sufficiently fine powders. The relative abundance of Fe associated with a specific Fe-bearing phases is therefore equal to the f-factor-normalized relative total area of each spectral pattern associated with that phase. Mössbauer spectra are split into component spectral patterns using computer programs to perform non-linear least squares fits where the line shape function (e.g., Lorentzian and Voigt) is a selectable parameter. The important results of fitting a spectrum are the Mössbauer parameters IS, QS, and B_{hf} and the relative areas for each component spectral pattern. The Mössbauer parameters serve to identify or constrain the mineralogical composition Fe-bearing phases, and the proportion of Fe associated with each specific phase is calculated from area and relative f-factor data. Large compilations of Mössbauer parameters for geologically relevant materials are publicly available [e.g., *Burns and Solberg*, 1990;

McCammon, 1995; *Stevens et al.*, 1998]. *De Grave and Van Alboom* [1991] report *f*-factors for Fe^{2+} and Fe^{3+} for a number of geologically relevant minerals.

2.4. Special Considerations for MER and Beagle-2

2.4.1. Backscatter Measurement Geometry

[18] Because of the complexity of sample preparation, backscatter measurement geometry is the choice for an in situ planetary Mössbauer instrument [e.g., *Morris et al.*, 1988; *Galazkha-Friedman and Juchniewicz*, 1989]. No sample preparation is required, because the instrument is simply presented to the sample for analysis. On MER, the MIMOS II sensor head is mounted on a robotic arm that places it in physical contact with the analysis target (e.g., rock or soil) [*Squyres et al.*, 2003]. MIMOS II is similarly mounted on Beagle-2 [*Sims et al.*, 2002].

[19] As discussed above, successful acquisition of Mössbauer spectra depends on accurate knowledge of the relative velocity of the source and sample. External vibrations that impart differential velocity components to the source and sample would degrade the quality of the Mössbauer spectrum. This degradation ranges from slight line broadening in mild cases to complete obliteration of the Mössbauer spectrum in severe cases. External vibrations are not generally a problem in laboratory settings because the sample and velocity transducer are rigidly held. On Mars, wind-induced vibrations are an obvious environmental factor that might degrade the quality of Mössbauer spectra. However, backscatter spectra obtained for hematite with a prototype MIMOS II instrument during field tests did not show detectable line broadening [*Arvidson et al.*, 1998]. The MER Instrument Deployment Device (IDD) has been designed to assure that velocity noise at the MIMOS II sensor head will not exceed 0.1 mm/sec [*Squyres et al.*, 2003].

2.4.2. Sampling Depth

[20] In addition to no requirement for sample preparation, backscatter measurement geometry has another important advantage. Emission of internal conversion electrons, Auger electrons, and X-rays, which occur along with the decay of the 14.4 keV γ-ray of ^{57}Fe, can also be used for Mössbauer measurements. For ^{57}Fe, internal conversion X-rays have an energy of 6.4 keV. In general, the comparative depths from which 6.4 keV X-rays and 14.4 γ-rays emerge in emission measurements depend on elemental composition. The importance of this difference in emission depths for an in situ Mössbauer spectrometer is that mineralogical variations that occur over the scale depths of the 14.4 and 6.4 keV radiations can be detected and characterized. Such a situation on Mars might arise for thin alteration rinds and dust coatings on the surfaces of otherwise unaltered rocks.

[21] Sampling depths can be estimated by calculation and by laboratory measurements. Figure 3 [after *Morris et al.*, 2000] shows by direct calculation that the sampling depth is ~50–200 μm for solid basaltic rock and ~500–2000 μm for fine-grained basaltic dust for 15 keV γ-rays (i.e., approximately the same energy as the 14.4 keV ^{57}Fe γ-ray). These calculations were confirmed by *Morris et al.* [2001b], who performed backscatter Mössbauer measurements of basaltic dust deposited to various thicknesses on rock substrates. These results show that we can "see" through a significant layer of dust coating and obtain mineralogical information about the underlying rock. *Morris et al.* [2000] show that the
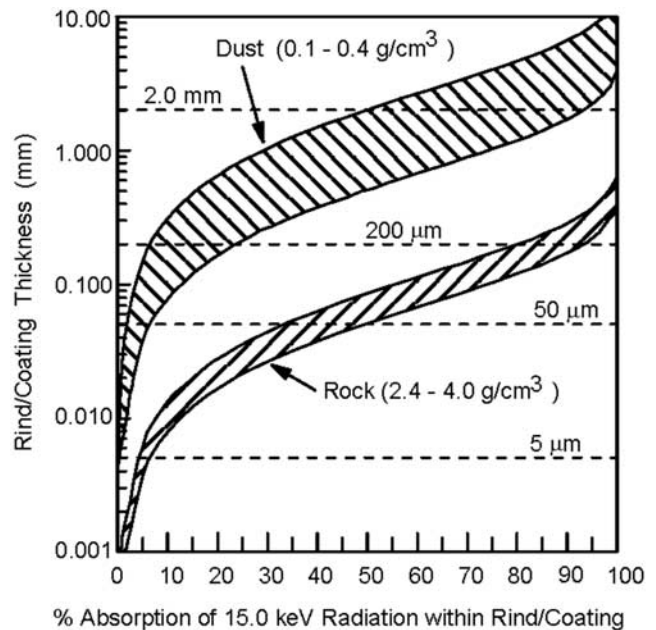

Figure 3. Calculated relationship between the thickness of an alteration rind and/or dust coating on a rock and the amount of 15.0-keV radiation absorbed in the rind/coating for densities of 0.4, 2.4, and 4.0 g/cm³ [after *Morris et al.*, 2000]. The bulk chemical composition of basaltic rock was used in the calculations, and the 15.0 keV energy is approximately the energy of the 14.4 keV γ-ray used in the Mössbauer experiment. The stippled area between densities of 2.4 and 4.0 g/cm³ is the region for dry bulk densities of terrestrial andesitic and basaltic rocks [*Johnson and Olhoeft*, 1984]. The stippled area between densities of 0.1 and 0.4 g/cm³ approximates the range of densities possible for Martian dust. The density of 0.1 g/cm³ is the density of basaltic dust deposited by air fall in laboratory experiments [*Morris et al.*, 2001b]. See color version of this figure in the HTML.

Mössbauer spectrum of interior rock can be detected through alteration rinds on rock surfaces.

2.4.3. Cosine Smearing

[22] Because instrument volume and experiment time must both be minimized for a planetary Mössbauer spectrometer, it is desirable in backscatter geometry to illuminate as much of the sample as possible with source radiation. However, this requirement at some point compromises the quality of the Mössbauer spectrum because of an effect known as "cosine smearing". The Doppler shift in energy of the 14.4 keV γ-rays incident on the sample depends not only on the velocity (v) of the source but also on the angle (θ) between the axis of source motion and the emission direction of source γ-rays. That is, the incident energy is proportional to the component of the source velocity along the γ-ray direction (v × cosθ) which gives the effect its name. The effect of cosine smearing on Mössbauer spectra is to increase the line width of Mössbauer peaks (lowers resolution) and to shift their centers outward (affects values of Mössbauer parameters). Therefore the diameter of the source "γ-ray beam" incident on the sample is a compromise between acceptable experiment time and acceptable velocity resolution.

[23] For coaxial symmetry, *Aramu and Maxia* [1970] calculated that when the ratio of the collimator radius and the distance between the source and the end of the collimator is ≤0.1, cosine smearing can be neglected. Note that the distortion in peak shape resulting from cosine smearing can be accounted for mathematically in spectral fitting routines, but the reduction in resolution can lead to irretrievable loss of information. *Riesenman et al.* [1969] derived a formula for the peak shape when cosine smearing is present for coaxial symmetry in transmission measurement geometry. A similar formula for conversion electron Mössbauer spectroscopy (CEMS) in backscattering geometry was described by *Klingelhöfer et al.* [1992]. Geometrical considerations are more complicated for MIMOS II, where backscatter measurement geometry is employed and the symmetry, although coaxial for the excitation process, is more complex for detection. *Held* [1997] solved this problem mathematically, and implemented the result in the fitting routines that we use.

2.4.4. Orientation Effects

[24] Because Martian surface material will be analyzed by Mössbauer spectrometers without sample preparation, variations in line intensity resulting from orientation effects are a strong possibility. This is especially the case for rocks with coarse grained mineral constituents, for example single-crystal phenocrysts of olivine whose dimensions are comparable to the Mössbauer source "beam diameter" (∼1.4 cm) that is incident on the sample. Orientation effects may also be present in Martian soil. For example, thermal emission spectra of the Meridiani Planum region that were obtained from Martian orbit by the Mars Global Surveyor Thermal Emission Spectrometer instrument have been interpreted in terms of an orientation effect for platy hematite crystals [*Christensen et al.*, 2000, 2001; *Lane et al.*, 2002]. This orientation effect would also be detected by Mössbauer spectroscopy [*Gonser et al.*, 1991]. Meridiani Planum is one of the landing sites for the MER rovers.

[25] Orientation effects and/or induced hyperfine splitting (or spectral broadening) are also important considerations for Mössbauer spectra acquired on material collected on the permanent magnets mounted on MER rover decks [*Madsen et al.*, 2003].

2.4.5. Temperature Variation

[26] Mössbauer parameters for many materials vary strongly with temperature. For laboratory instruments, sample temperature can be changed and held at different temperatures by ovens and cryostats for as long as necessary for determination of Mössbauer parameters as a function of temperature. During a typical overnight Mössbauer experiment on Mars, however, the sample temperature will vary by many tens of degrees. To both ensure the quality of Martian Mössbauer spectra (i.e., prevent line broadening from temperature dependent Mössbauer parameters) and to measure any temperature dependence in Mössbauer parameters (which aids in phase identification), a Mössbauer spectrometer on Mars must be able acquire and separately store spectra as a function of temperature.

3. MIMOS II Instrument Description

3.1. Design Overview

[27] Because of mission constrains for minimum mass, volume, and power consumption, the MIMOS II is extremely miniaturized compared to standard laboratory Mössbauer spectrometers and is optimized for low power consumption and high detection efficiency [*Klingelhöfer et al.*, 1998; *Klingelhöfer*, 1999]. All components were selected to withstand high acceleration forces and shocks, temperature variations over the Martian diurnal cycle, and cosmic ray irradiation. Because of restrictions in data transfer rates, most instrument functions and data processing capabilities, including acquisition and separate storage of spectra as a function of temperature, are performed by an internal dedicated microprocessor (CPU) and memory. The dedicated CPU is also required because most Mössbauer measurements will be done at night when the rover CPU is turned off to conserve power. High detection efficiency is extremely important in order to minimize experiment time. Experiment time is also minimized by using as strong a main ^{57}Co/Rh source as possible. Because the half-life of ^{57}Co (271 days) is not much longer than the 6–7 month duration of the journey to Mars, this implies a design and schedule that allows the source to be manufactured, delivered, and mounted in MIMOS II as close to launch as possible. Instrument internal calibration is accomplished by a second, less intense radioactive source mounted on the end of the velocity transducer opposite to the main source and in transmission measurement geometry with a reference sample. For MER, the spectrometer can also be calibrated with the magnetite Compositional Calibration Target (CCT) which is mounted on the rover body [*Squyres et al.*, 2003].

[28] Physically, the MIMOS II Mössbauer spectrometer has two components that are joined by an interconnect cable: the sensor head and electronics printed-circuit board. On MER, the sensor head is located at the end of the IDD and the electronics board is located in an electronics box inside the rover body. On Mars-Express Beagle-2, the sensor head is mounted on a robotic arm integrated to the "Position Adjustable Workstation" (PAW) instrument assembly. The sensor head (Figures 4 and 5) contains the electromechanical transducer (mounted in the center), the main and reference ^{57}Co/Rh sources, collimator (multilayered radiation shields), detectors and their preamplifiers and main (linear) amplifiers, and a contact plate and sensor. The contact plate and sensor are used in conjunction with the IDD so that a small preload can be applied to hold the sensor head assembly firmly against the analysis target. The electronics board contains power supplies/conditioners, the dedicated CPU (a 8051 type microprocessor), different kinds of memory, firmware, and associated circuitry for instrument control and data processing.

3.2. Mössbauer Sources, Shielding, and Collimator

[29] To minimize experiment time, the highest possible source activity is desirable, with the constraint that the source line width should not increase significantly (maximum by a factor of 2–3) over the ∼9–12 months duration of the mission. Calculations and tests indicate an optimum specific activity for ^{57}Co at 1 Ci/cm^2 [*Gummer*, 1988; *Evlanov et al.*, 1993]. Sources of ∼330 mCi ^{57}Co/Rh with a specific activity close to this value and extremely narrow source line width (<0.13 mm/s at room temperature) given the high activity, were produced by Cyclotron Co. Ltd. (Russia) in custom made space-qualified Ti-holders, tested successfully, and mounted in flight instruments approxi-
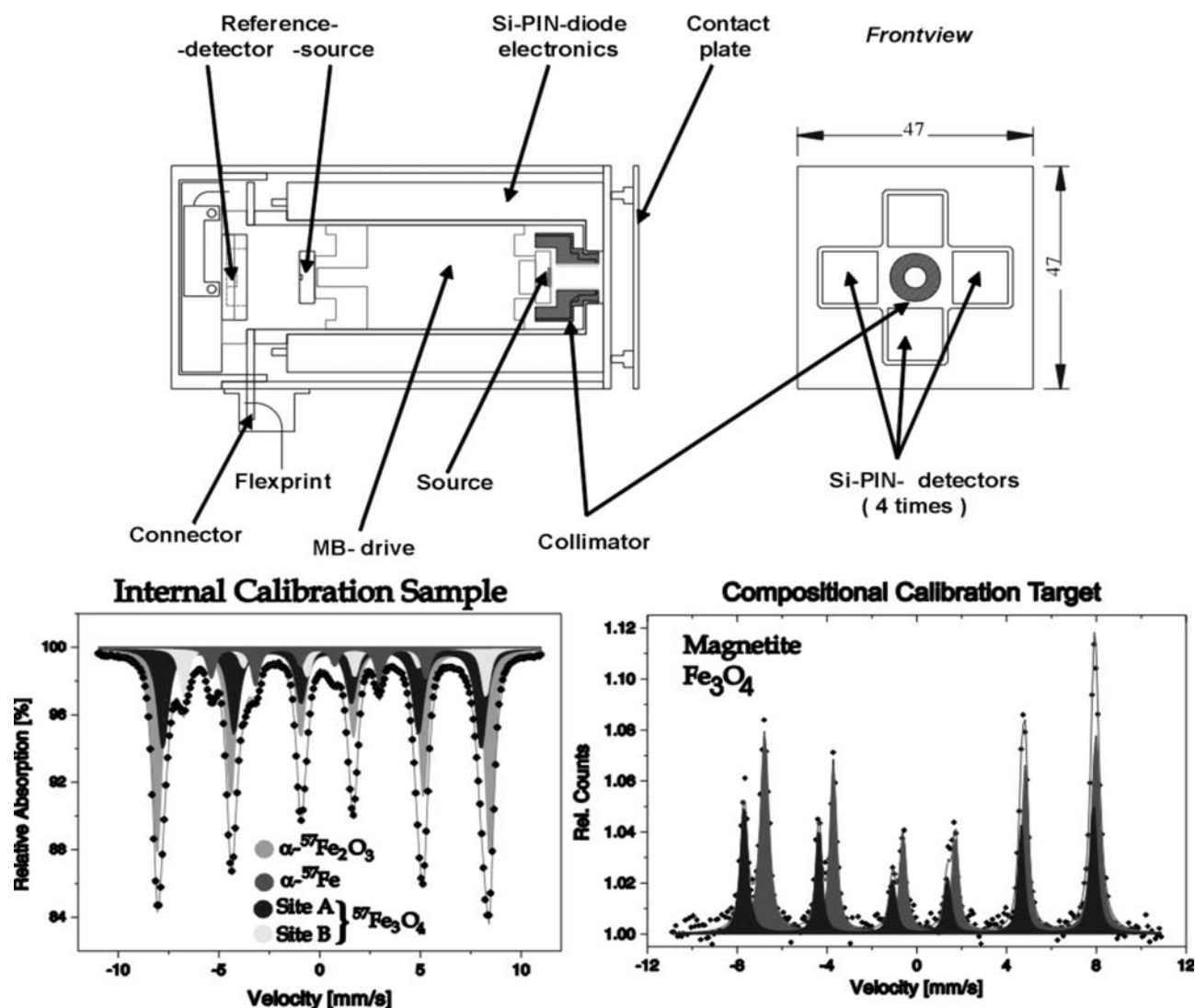
Figure 4. Schematic drawing of the MIMOS II Mössbauer spectrometer. The velocity transducer to which both the reference and main ^{57}Co/Rh sources are attached is indicated on the drawing as "MB-drive". The transmission spectrum for a prototype internal reference standard shows the peaks corresponding to hematite (α-Fe$_2$O$_3$), α-Fe^0, and magnetite (Fe$_3$O$_4$). The internal reference standards for MIMOS II flight units are only hematite and metallic iron. The backscatter spectrum for the magnetite MER compositional calibration target (CCT), which is mounted on the rover deck and is available to the MIMOS II during the mission, is also shown. See color version of this figure in the HTML.

mately 90 days prior to launch. No additional line broadening will result at lower temperatures on Mars with the rhodium matrix.

[30] Very important is an effective shielding of the detector system from direct and cascade radiation from the ^{57}Co/Rh source. A graded shield consisting of concentric tubes of brass, tantalum, and lead was selected. The thickness and the shape of different parts of the shielding were optimized so that nearly no direct 122 and 136 keV radiation (emitted by the ^{57}Co source) is in a direct line with the detectors.

[31] The shielding also acts as the collimator which fixes the diameter of the target that is illuminated by γ-rays. As discussed previously, this diameter is as large as possible to minimize experiment time within the constraint of accept-

able cosine smearing [*Klingelhöfer et al.*, 1992]. The measure used for acceptable cosine smearing was the ability to reliably resolve the strongly overlapping spectra of hematite and maghemite in a 1:1 mixture of those oxides. A series of experiments with this mixture and the pure oxides were conducted at constant source intensity and variable collimator diameters between 4.5 and 7.1 mm, which corresponds to an illumination diameter of $\sim$12 and $\sim$17 mm, respectively [*Schröder*, 2001]. The spectra were analyzed using the fitting routine developed by *Held* [1997]. Analysis of the mixture spectra reproduced the Mössbauer parameters for and relative proportions of the individual oxide components for collimator diameters of 4.5 and 5.6 mm. For collimator diameters of 6.2 and 7.1 mm, the calculated and actual relative proportions of the oxides
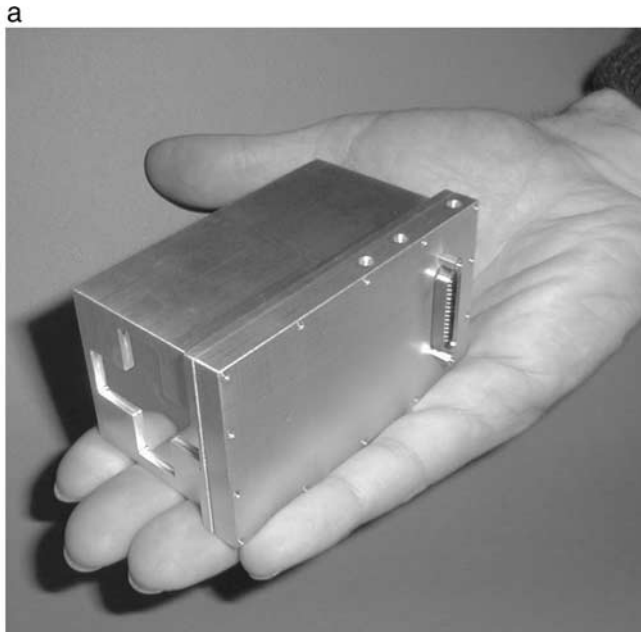
a

Figure 5. (a) External view of the MIMOS II sensor head without contact plate assembly. (b) MIMOS II sensor head (without contact plate assembly) with dust cover taken off to show sensor head interior. At the front, the end of the cylindrical collimator is surrounded by the four Si-PIN detectors that detect the radiation emitted by the sample. The metal case of the upper detector is removed to show its associated electronics. The electronics for all four detectors is the same. The Mössbauer drive is inside (in the center) of this arrangement, and the reference channel is located on the back side in the metal box shown in the photograph. (c) View of the MIMOS II sensor head mounted on the turret with the ASI (Alliance Spacesystems Inc., California) contact plate assembly. See color version of this figure in the HTML.

differ significantly. Therefore a collimator diameter of 5.6 mm was selected for MIMOS II flight instruments. This diameter limits the maximum γ-ray emission angle to ∼25° and gives a "beam diameter" of ∼14 mm on the sample. As expected, because cosine smearing was observed, the ratio of collimator radius to the distance between the source and the end of the collimator (∼0.25) is considerably larger than the <0.1 value required for the effect to be negligible.

3.3. Drive System

[32] The simplest way to meet volume and weight constraints was to scale down drive systems we have built for laboratory instruments for many years [*Kankeleit*, 1964, 1975]. We constructed a drive system which had about one fifth the size of a standard laboratory system. It has a diameter of 22 mm, a length of 40 mm, and ∼50 g mass [*Teucher*, 1994].

[33] The MIMOS II design is based on a rigid aluminum tube connection between drive and the velocity pick-up coils in the double-loudspeaker arrangement with good electrical and magnetic shielding between the two coils to avoid crosstalk. The intense main ^{57}Co/Rh source is mounted at one end of the aluminum tube, and the weaker

source for the reference absorber is mounted at the other end. The short tube guarantees a fast transfer of information with the velocity of sound in the aluminum and thus a minimum phase lag and a high feedback gain margin. Fortunately, and despite the increase of unwanted crosstalk resulting from the smaller distance between the coils, the crosstalk relative contribution is still less than 0.01% in the frequency domain of the triangular waveform and is therefore negligible. The system is equipped with SmCo permanent magnets and was optimized to give a homogeneous and high magnetic field in the coil gaps. To do this, the specialized computer program PE2D, designed to calculate magnet systems for charged particle storage rings in high energy physics, was used for calculation and optimization of the drive magnet system. We found good correspondence between calculated and experimental magnetic field measurements that were performed using a Hall sensor [*Teucher*, 1994].

[34] The drive operates at a frequency of ∼25 Hz, which is also its main resonance (Figure 6). This low frequency allows a broad bandwidth for the closed loop system, and good performance with a triangular reference signal, but requires rather soft Kapton springs. As a consequence, rotation of the drive from horizontal to vertical position in Earth gravity leads to a shift of about 0.4 mm from the equilibrium position of the tube. However, the resulting non-linearity between velocity and pickup voltage remains <0.1% at room temperature. Although this shift could be compensated by a DC current, no correction is needed for a mission to Mars where the gravity forces are smaller by a factor of ∼3. In order for the drive to operate over expected Martian surface temperatures (80–283 K), it was necessary to degrade the velocity linearity from 0.1% to ∼3%, which is correctable after calibration with software.

[35] The design provides limiters to avoid destruction of the Kapton springs during the large accelerations associated with launch and landing. Vibration and shock tests of the drive system with levels up to, and slightly exceeding the specifications for both MER and Beagle-2 missions were successfully performed.

3.4. Detector System and Electronics

[36] The main disadvantage of the backscatter measurement geometry employed by MIMOS II is the secondary radiation caused by primary 122 keV and 136 keV radiation from the decay of ^{57}Co source. To reduce the background at the energies of the 14.4 keV γ-ray and the 6.4 keV X-ray lines, a detector with good energy resolution is required. In addition, a detector system covering a large solid angle is needed to minimize data acquisition time. Good resolution is even more important should it prove possible to use these detectors for elemental analysis with the X-ray fluorescence technique (i.e., using the pulse height analysis (PHA) spectra that are also acquired as a part of our measurement procedure). For this reason, four Si-PIN-diodes with a 10 × 10 mm^2 active area were selected as detectors [*Weinheimer et al.*, 1992; *Held*, 1993; *Held et al.*, 1993] instead of gas-counters as considered by other authors [*Prilutskii*, 1990; *Agresti et al.*, 1992]. A detector thickness of about 400-500 μm is a good choice according to our calculations and experience. The energy resolution is ∼1.0–1.5 keV at room temperature, and it improves at lower temperatures. The
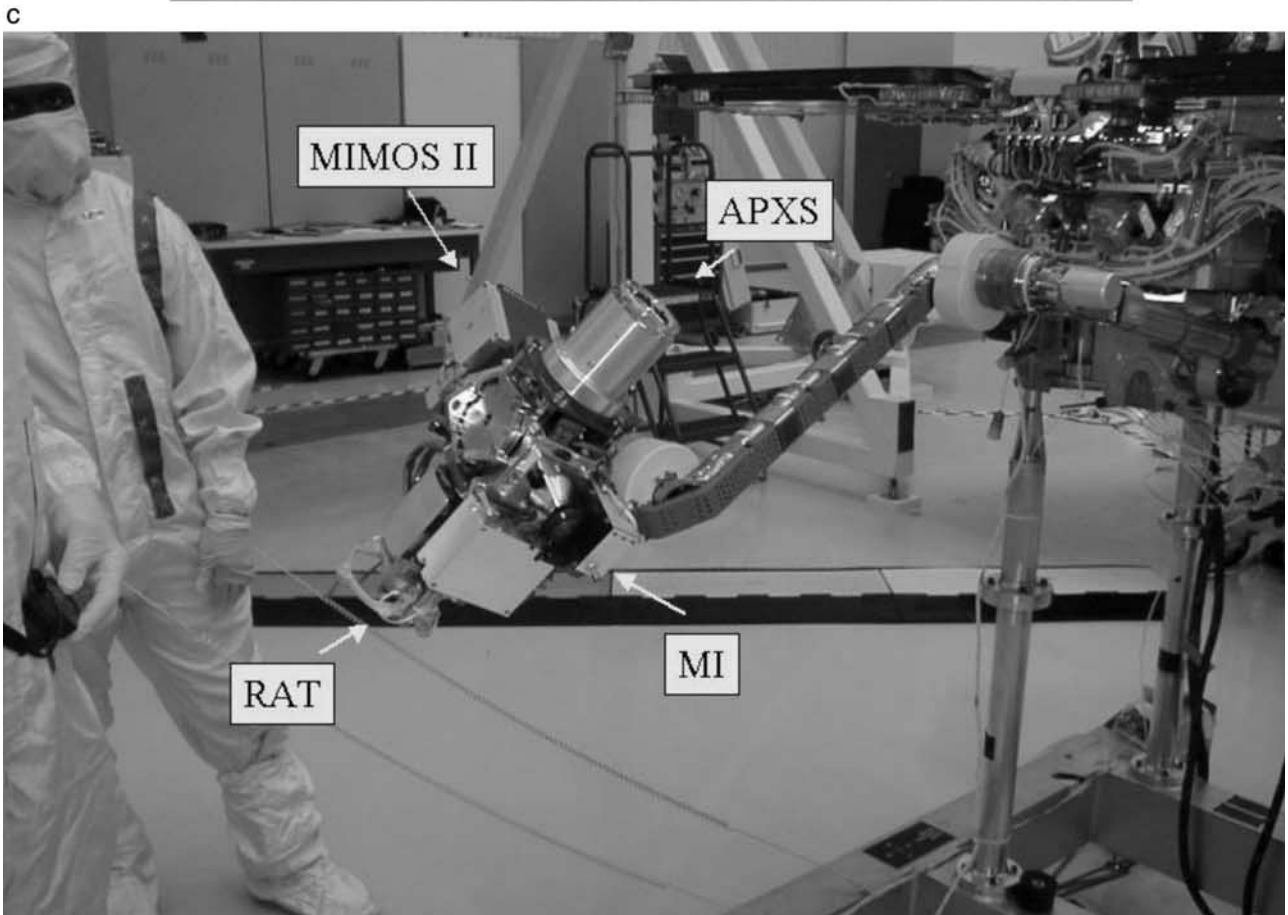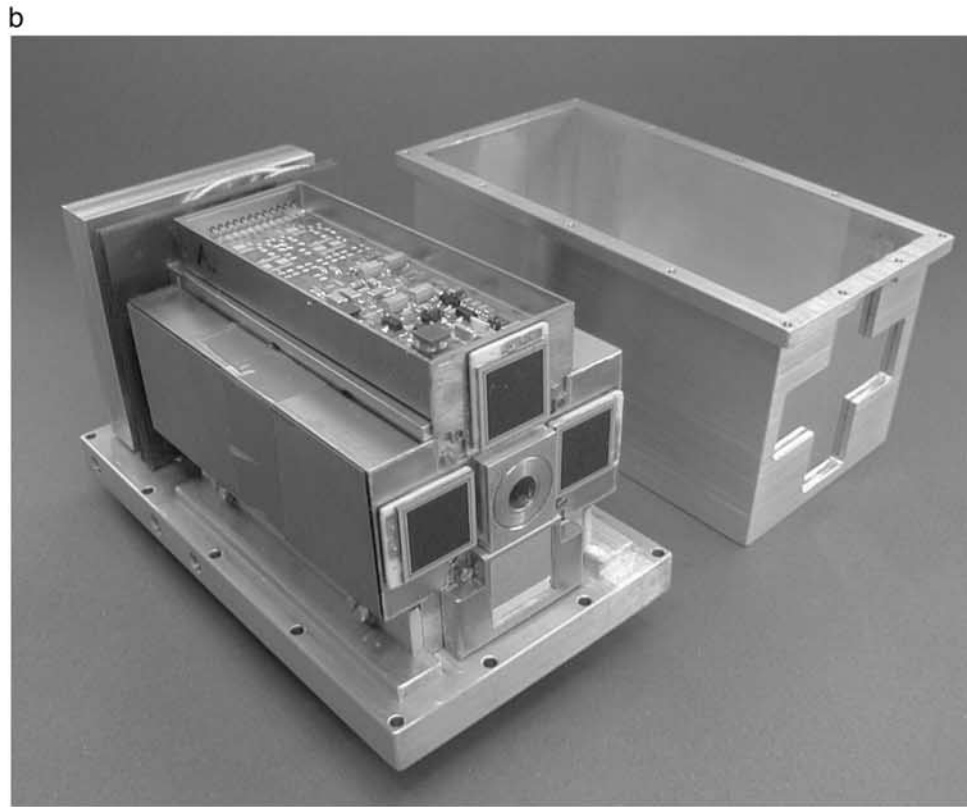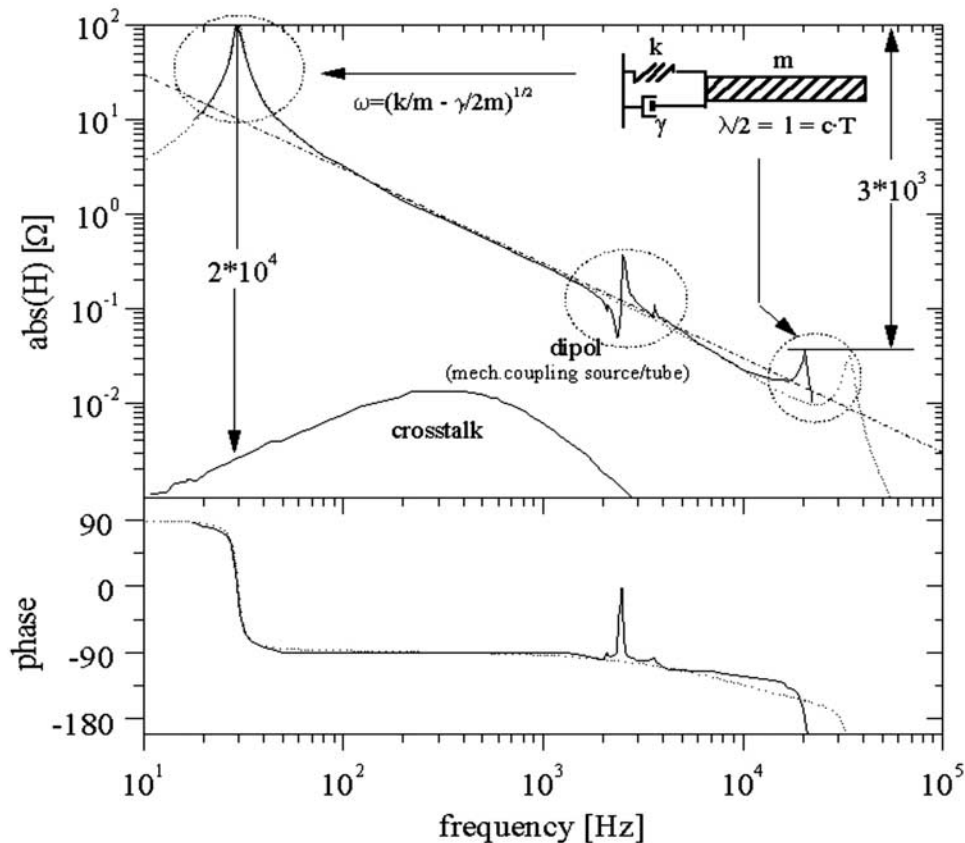
Figure 5. (continued)

Figure 6. Transfer function for MIMOS II velocity transducer.

efficiencies at 6.4 and 14.4 keV are nearly 100% and about 70%, respectively [*Held*, 1993; *Held et al.*, 1993].

[37] The 100 V DC bias voltage for the detector diodes is generated by high frequency cascade circuitry with a power consumption of less than 5 mW. Noise contributions are minimized by incorporating a preamplifier-amplifier-SCA system for each individual detector.

[38] Spectra of ^{57}Co/Rh radiation backscattered from an aluminum (Al) and a stainless steel (SS) plate (same recording times) are shown in Figure 7. A continuum is seen above 122 keV resulting from the few 692 keV γ-rays which are not completely absorbed in the shielding. Although no photo peak appears at 122 keV, this radiation shows up as a broad Compton distribution being more intense for the lower Z aluminum. A second Compton distribution originates in the detector itself as seen in the rising slope starting below 40 keV. The peak at 22.1 keV results from the silver (Ag) backing of the detector. Below this energy the 14.4 keV Mössbauer resonance line and also the 6.4 keV X-ray line dominate in SS at zero velocity, in contrast to Al where only the (14.4–0.4) keV Compton scattered line appears.

[39] In addition to the four detectors used to detect backscattered radiation from the sample, there is a fifth detector to measure the transmission spectrum of the reference absorber (α-^{57}Fe^0 plus α-^{57}Fe$_2$O$_3$). Sample and reference spectra are recorded simultaneously, and the known temperature dependence of the Mössbauer parameters of the reference absorber can be used to give a measurement of the

average temperature inside the sensor head, providing a redundancy to measurements made with the internal temperature sensor.

3.5. Temperature Measurement

[40] MIMOS II has three temperature sensors: one on the electronics board in the Rover warm electronics box and two on the sensor head (Analogue Devices AD590). One temperature sensor in the sensor head is mounted near the internal reference absorber, and the measured temperature is associated with the reference absorber and the internal volume of the sensor head. The other sensor is mounted outside the sensor head at the contact ring assembly. It gives the approximate analysis temperature for the sample on the Martian surface. This temperature is used to route the Mössbauer data to the different temperature intervals (maximum of 13, with the temperature width software selectable) assigned in memory areas. An example of a simulated overnight experiment on Mars is shown in Figure 8 for eight temperature intervals using the CCT as the target. The eight backscatter spectra collected from the target and the corresponding eight velocity reference spectra are in Figures 8a and 8b, respectively. In case of contact-ring temperature sensor failure, the internal temperature sensor would be used (software selectable).

[41] During measurements, a temperature log is acquired for all three sensors. Temperature measurements are done approximately every 5 min (software selectable from ~10 s to ~40 min). MIMOS II can accumulate up to 256 temper-
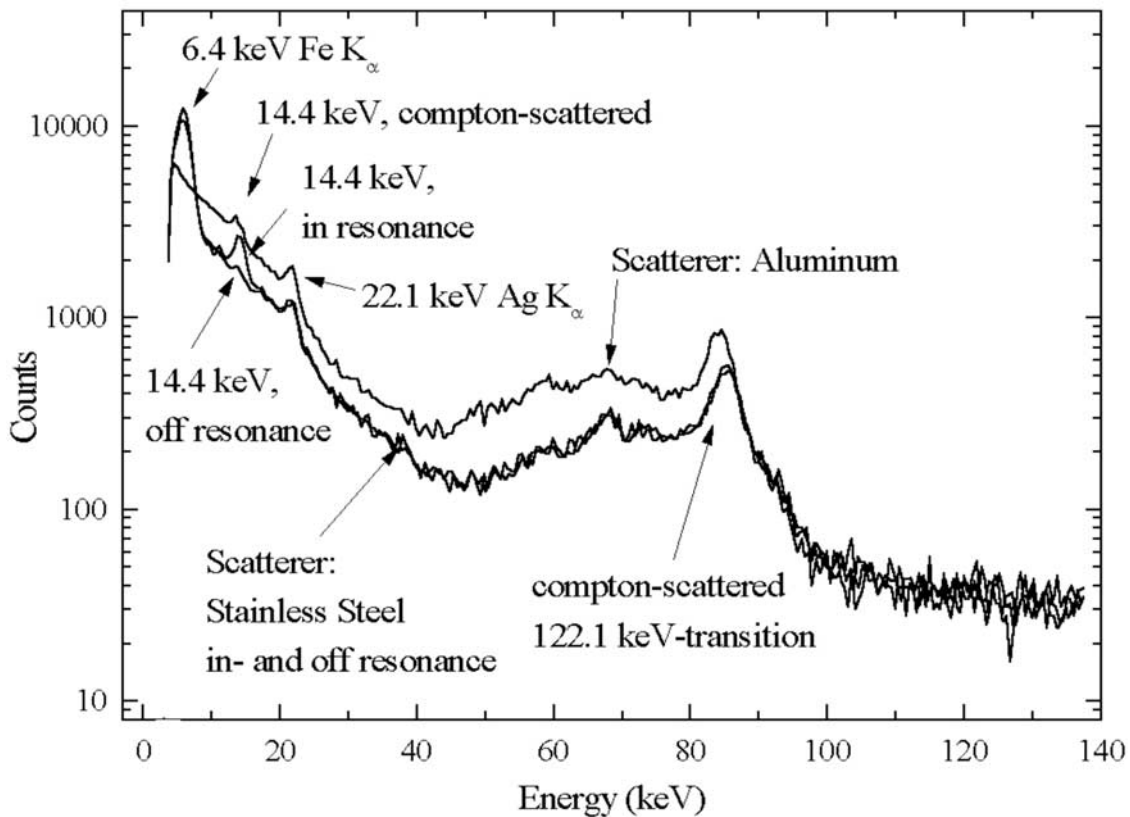
Figure 7. Pulse-height analysis (PHA) spectrum for $^{57}Co/Rh$ backscattered non-resonantly and/or resonantly from aluminum and stainless steel plates. See color version of this figure in the HTML.

ature records corresponding to a total integration time of ~21 hours.

3.6. Operation Modes and Software
3.6.1. MIMOS II Operational Modes
[42] The instrument can be operated in six different modes depending on the nature of the requirement. (1) Mössbauer temperature-dependent mode. Mössbauer sample and reference spectra are collected and stored as a function of up to 13 temperature intervals. The temperature ranges are variable and can be changed during mission operations. (2) Mössbauer temperature independent mode. Mössbauer and reference spectra are collected irrespective of the sample or reference temperature. (3) Energy mode. PHA spectra are collected to determine detector performance and to make changes in energy-window settings. (4) Engineering mode. The drive differential signal, i.e., the error signal (pickup voltage - velocity reference voltage), is collected to determine the velocity drive performance. (5) Idle mode. In this mode, no operations are performed. (6) Standard mode. This mode is used for normal operations. It consists of the Engineering, Energy, and Mössbauer temperature dependent modes commanded sequentially.
3.6.2. Data Structure, Temperature Log, and Backup Strategy
[43] One Mössbauer spectrum consists of 512 velocity channels (3 bytes/channel). One temperature interval consists of five Mössbauer spectra (one for each detector). There are 13 temperature intervals with selectable width. Thus MIMOS II can accumulate up to 65 Mössbauer

spectra during one experiment session on Mars. All Mössbauer, energy, engineering, and temperature data taken during this session are stored in a volatile SRAM memory (128 KB) on the MIMOS II electronics board.

[44] Firmware parameters and the instrument logbook are stored in the non-volatile memory ferroelectric RAM (FRAM) on the electronics board. There are three individual FRAMs on the MIMOS II electronics board with three identical copies of these parameters to ensure parameter integrity. The copies are verified and compared to each other from time to time to verify they are identical. If one copy deviates from the other two, it will be replaced by a copy of the two other still identical parameter sets. All parameters can be adjusted during mission operations.

[45] To minimize risk of data loss because of power failure or other reasons, the Mössbauer data are copied to a non-volatile EEPROM memory every 9 min (software selectable). As the size of the EEPROM is smaller than the SRAM, the EEPROM can accumulate only up to ten Mössbauer spectra as a subset of the data from the SRAM. These spectra are obtained from the SRAM according to a pre-defined summation strategy.

3.7. Velocity and Energy Calibration
3.7.1. Velocity Calibration
[46] The interpretation of acquired Mössbauer spectra is impossible without knowing the drive velocity and in particular the maximum velocity value precisely at any given time. Mössbauer drive velocity calibration for MIMOS II is rather straightforward and can done in three different ways,
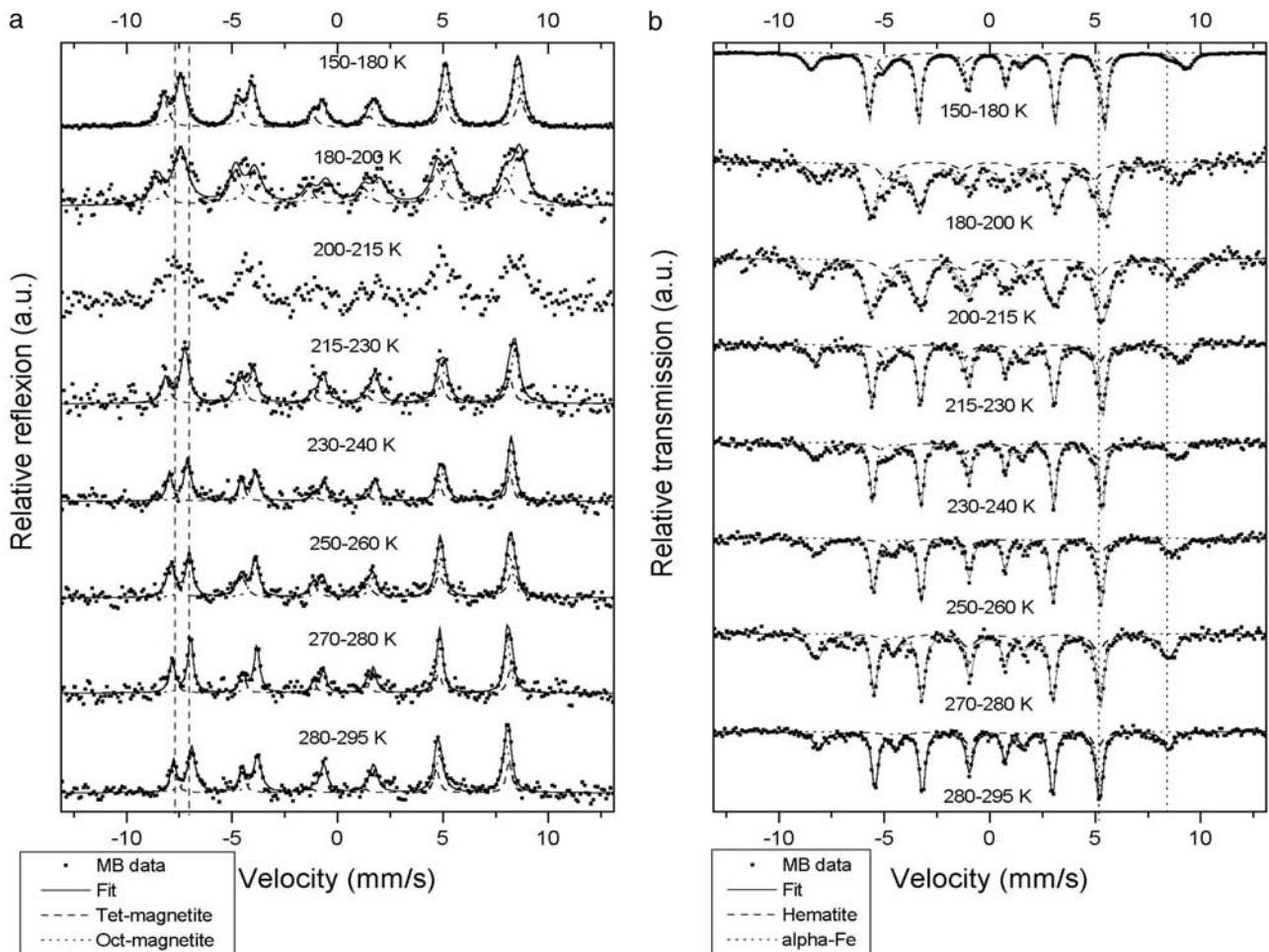
Figure 8. (a) Backscatter MIMOS II spectra collected in eight temperature intervals on the CCT target during a simulated overnight Mössbauer experiment on Mars. (b) Corresponding transmission spectra for the velocity reference sample. See color version of this figure in the HTML.

thus ensuring redundancy. Prior to flight each individual drive system was calibrated as function of the software velocity settings (y axis in Figure 9 labeled "Internal V_{max} value") by measuring in backscattering mode an α-iron foil standard at different software velocity range settings. For each setting the maximum drive velocity was preset by firmware and the corresponding Mössbauer spectrum acquired. Fitting the acquired Mössbauer spectrum using the well-known parameters of the α-iron foil then yielded the real velocity for that particular setting. In that way a calibration curve for the real "Maximum Velocity" value as function of the internal software velocity setting was obtained for each Mössbauer unit. As an example the results for a MIMOS II flight unit are presented in Figure 9. This procedure was repeated at different temperatures.

[47] During the mission, the magnetite CCT (Compositional Calibration Target) will be measured in several runs to verify the functionality of MIMOS II. The well-known Mössbauer parameters of magnetite can be used for velocity calibration. These kinds of measurements were done in the laboratory with the flight units as a function of temperature, to be used as reference for the measurements on Mars. Figure 8a shows a Mössbauer spectrum for the CCT.

[48] The primary method for velocity calibration is the internal reference target and detector configured in trans-

mission measurement geometry (Figure 4). The reference target is a mixture of α-Fe^0 (metallic iron, 30% enriched ^{57}Fe) and α-Fe$_2$O$_3$ (hematite, 95% enriched ^{57}Fe), and its Mössbauer spectrum is measured automatically during each backscatter experiment. Each component of the reference target has well-known Mössbauer parameters, so that fitting of reference spectra enables velocity calibration for each individual measurement done in backscatter geometry, ensuring that the actual drive velocity is always well defined, regardless of prevailing environmental conditions.

3.7.2. Detector Calibration

[49] Careful energy calibration on each detector was done to achieve optimal detection rate. Each sensor head was temperature cycled (153 K–293 K). During cycling, energy spectra were measured. As a result of analysis of these spectra, optimal firmware parameters were calculated for each detector and each temperature window. During operation, instrument firmware will adjust those parameters depending on temperature, thus ensuring best detector performance.

4. Validation of MIMOS II Performance

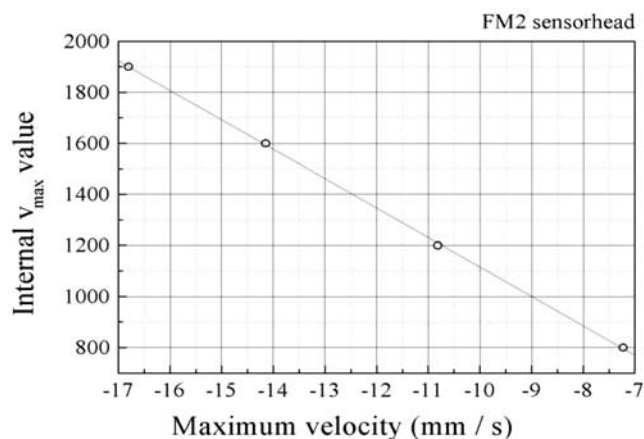[50] In this section, we compare MIMOS II and laboratory Mössbauer spectra and parameters derived from those

Figure 9. Preflight MIMOS II sensor head "Maximum Velocity" calibration. Prior to flight each individual drive system was calibrated as a function of the software velocity settings (y axis labeled "Internal Vmax value") by measuring in backscattering mode an α-iron foil standard at different software "Maximum Velocity" range settings. Fitting the acquired Mössbauer spectrum using the well-known parameters of the α-iron foil then yielded the real velocity for that particular setting. In that way the calibration curve for the real "Maximum Velocity" value as function of the internal software velocity setting was obtained for each Mössbauer unit. As an example, the results for a MIMOS II flight unit are presented here. Negative maximum velocity values (x axis) are given because they belong to channel 1 in the Mössbauer spectrum. This procedure was repeated at different temperatures.

spectra to document the performance of MIMOS II. We also report initial measurements to determine the detection limit of the instrument for silicate and oxide phases against palagontic tephra, a Martian bright regions analogue [*Morris et al.*, 2000].

[51] Figure 10 shows Mössbauer spectra (293 K) for five Martian analogue samples obtained in transmission geometry using a laboratory spectrometer and 10 mg/cm^2 sample thickness (relative to Fe) and in backscatter geometry using a prototype MIMOS II instrument and pure, undiluted powders of the samples. The MIMOS II spectra are 512 channels of mirror-imaged spectra folded to 256 channels. The laboratory spectra are 1024 channels of mirror-imaged spectra folded to 512 channels [e.g., *Morris et al.*, 2000]. For purposes of comparison, the laboratory spectra were inverted and overlaid on the backscatter spectra. The backscatter and inverted transmission spectra nearly exactly coincide. In particular, note that peaks in the backscatter spectra are not obviously skewed away from zero velocity relative to the corresponding peaks in the transmission spectra and that the corresponding relative peak heights are approximately the same. These two observations show that cosine smearing may not be a very significant consideration for MER backscatter spectra, particularly in the velocity region between -4 and $+4$ mm/s where most ferrous and ferric doublets occur. A reason for this might be that, because of fabrication tolerances, the actual collimator diameter is smaller and the actual distance between
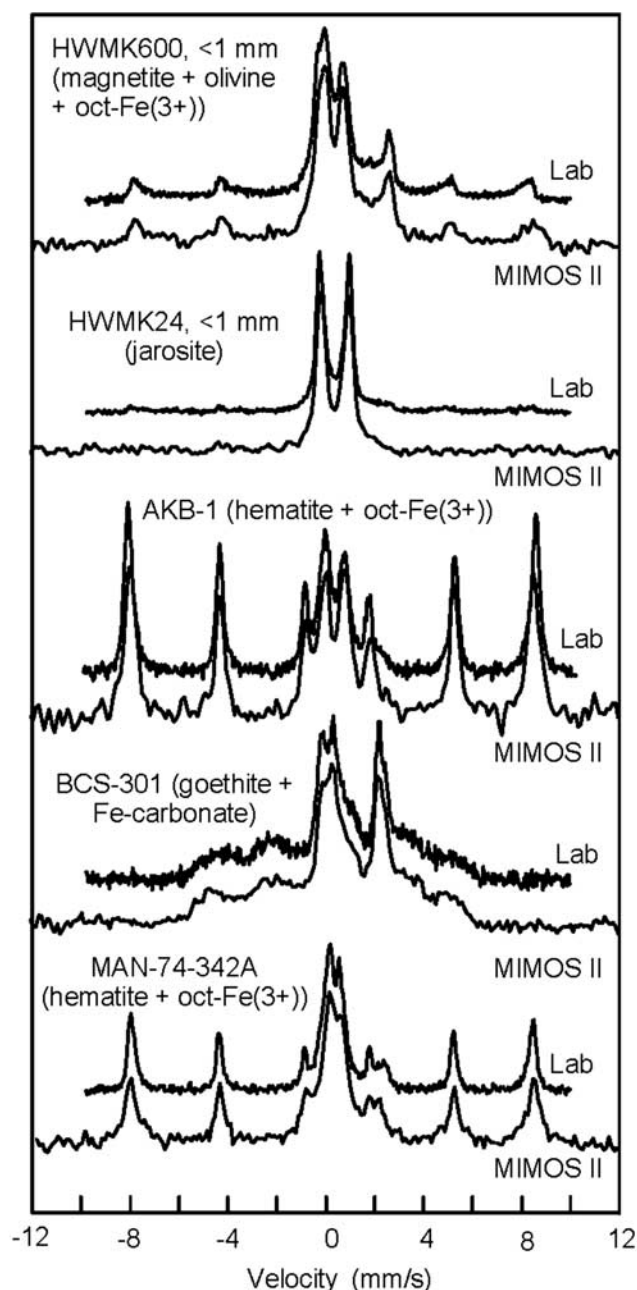

Figure 10. Comparison of Mössbauer spectra (293 K) in backscatter and transmission geometries for Martian analogue samples. Backscatter spectra (512 velocity channels folded to 256 channels) were obtained using a prototype MIMOS II spectrometer, and transmission spectra (1024 velocity channels folded to 512 channels) were obtained using a laboratory spectrometer. The overlay was done by inverting the transmission spectra, overlapping the baselines, and normalizing maximum intensities to the same value. HWMK600 and HWMK24 are the <1 mm size fractions of palagonitic and jarositic tephra from Mauna Kea Volcano (Hawaii). AKB-1 and BCS-301 are an amygdaloidal basalt (Michigan) and an iron ore (Lincolnshire, England). MAN-74-342A is an impact melt rock from Manicougan Crater (Quebec, Canada). Mössbauer spectra are adapted from *Morris et al.* [1995, 1996, 1998b, 2000]. MIMOS II and laboratory spectra are offset for clarity. See color version of this figure in the HTML.

the source and the end of the collimator is larger than the values assumed for calculation of the cosine smearing effect. The observations also show that theoretical peak intensity ratios in transmission measurements (e.g., 3:2:1:1:2:3 for sextets) are applicable for backscatter measurements, at least for these kinds of samples.

[52] Mössbauer spectra for two reference rock slabs are shown in Figure 11, and the derived Mössbauer parameters are given in Table 1. The Mössbauer parameters for AREF043 and AREF121 are consistent with literature values for magnetite and hematite, respectively [e.g., *Stevens et al.*, 1998], and these two oxides are the only iron bearing phases detected in these two rock samples. The AREF043 spectrum was acquired in 49 hours with a 25 mCi source intensity. This is the equivalent of a 12 hour integration at the nominal source intensity at Mars during the MER mission. The AREF121 spectrum was acquired in 92 hours with a source activity of 30 mCi, corresponding to about 27 hr at 100 mCi (nominal at Mars). This is a higher quality spectrum than will likely be obtained on Mars. Note that the IS and QS Mössbauer parameters that are calculated with and without inclusion of cosine smearing are nearly the same within error. As expected, the values of B_{hf} without the cosine smearing correction are somewhat too large (~0.3 T), and therefore for the analysis of MIMOS II spectra the cosine smearing correction needs to be applied.

[53] To estimate detection limits for various Mars-relevant iron-bearing phases, we mixed (by ultrasonic dispersal in ethanol followed by air drying) various quantities of those phases (e.g., hematite, goethite, and olivine) with the <150 μm size fraction of palagonitic tephra HWMK600, which is a Martian bright regions spectral analogue [*Morris et al.*, 2000]. Figure 12 shows Mössbauer spectra obtained by an engineering model MIMOS II for mixtures of the palagonite with well-characterized submicron powders [*Morris et al.*, 1985] of hematite (HMS3 and HMS12) and magnetite (MTS4). Although additional measurements are needed (for both oxide and silicate phases) at different mixing ratios, 10 hr integrations (comparable to overnight experiments on Mars) at a source intensity of $\sim80-100$ mCi are sufficient to detect hematite and magnetite at the 1–2% level against a background of palagonitic tephra.

5. Operational Considerations

5.1. Planned Measurements

[54] The instruments on the Athena payload [*Squyres et al.*, 2003] were chosen to be complementary to one another, and wherever possible the targets analyzed by the Mössbauer spectrometer will be examined by all the other instruments on the payload as well. There is particular synergy between the MIMOS II and the APXS. Both these IDD-mounted instruments will be normally operated during the overnight period, with the split in analysis time depending on the information available on the target. The APXS provides the elemental composition for the target, and MIMOS II provides the mineralogical composition, including the Fe^{2+}/Fe^{3+} ratio so that concentrations of FeO and Fe_2O_3 can be include in the major element analyses. Images of the target, taken before and after MIMOS II and APXS measurements, by the Microscopic Imager (MI) [*Herkenhoff et al.*, 2003] document the material actually analyzed. Images taken by the

front Hazcams [*Maki et al.*, 2003] document instrument placement on the target. Images and multispectral data obtained by Pancam [*Bell et al.*, 2003] and Mini-TES [*Christensen et al.*, 2003] complete full characterization of the target by the Athena instrument suite.

[55] Targets for Mössbauer analysis for the mineralogical composition of Fe-bearing phases the relative distribution of Fe and its oxidation states among those phases, are the exposed surfaces of soil and rock, interior regions of rock exposed by the Rock Abrasion Tool (RAT) [*Gorevan et al.*, 2003], subsurface soil exposed by trenching [*Arvidson et al.*, 2003], and the two magnets mounted on the rover deck [*Madsen et al.*, 2003]. In the case of the magnets, it is known from Viking [e.g., *Hargraves et al.*, 1979] and Mars Pathfinder [e.g., *Hviid et al.*, 1997; *Madsen et al.*, 1999] that Martian aeolian dust is magnetic, but the composition of the magnetic phase or phases is not known. When the dust buildup on the magnets is sufficiently large, as determined using Pancam, the IDD will be used to place MIMOS II directly against the magnets, providing what should be a definitive identification of the magnetic phases present. Fine-grained material produced by the RAT, if present in sufficient lateral extent and depth, provides a target that is representative of the volume excavated and for which mineral orientation effects are likely not present. The relatively high penetration depth of the 14.4 keV Mössbauer radiation (Figure 3) means that it may be possible to obtain mineralogical information about unaltered rock without removing exterior rinds or dust coverings with the RAT.

[56] The Mössbauer instrument is less contamination sensitive to dust than the APXS [*Rieder et al.*, 2003] or the Microscopic Imager [*Herkenhoff et al.*, 2003], which are the other two instruments on the IDD. Therefore, for soft and/or dirty targets the MIMOS II contact sensor may sometimes be used as a "blind man's cane", helping to establish target location in IDD coordinates so that the other instruments can be placed with less risk of contamination.

[57] Because the MIMOS II instrument is exposed to the Martian environment, there is the possibility that dust will accumulate on detector and collomator-exit windows. There are no provisions designed into the instrument to physically remove the dust. However, because the windows are electrically conductive and they are irradiated continuously by electromagnetic radiation from the Mössbauer source, dust accumulation is expected to be small. Dust coatings on window surfaces results primarily in mass attenuation of photons, which increases the experiment time to get the same quality of spectrum relative to the case for no dust.

[58] In some instances, it may be possible for MIMOS II to achieve a signal-to-noise ratio that is adequate for answering key scientific questions in a time much less than the nominal experiment time of 6–12 hr during the overnight period. This will be particularly true early in the mission when radiation source strength is greatest and for targets with high Fe contents. Where appropriate, then, the Mössbauer may be used in a "touch and go" mode [*Squyres et al.*, 2003], in which a short integration is performed at the start of a sol, followed by other rover activities that may include driving.

5.2. Data Analysis

[59] For a Mössbauer experiment on any target, MIMOS II stores in memory for return to the Earth the following
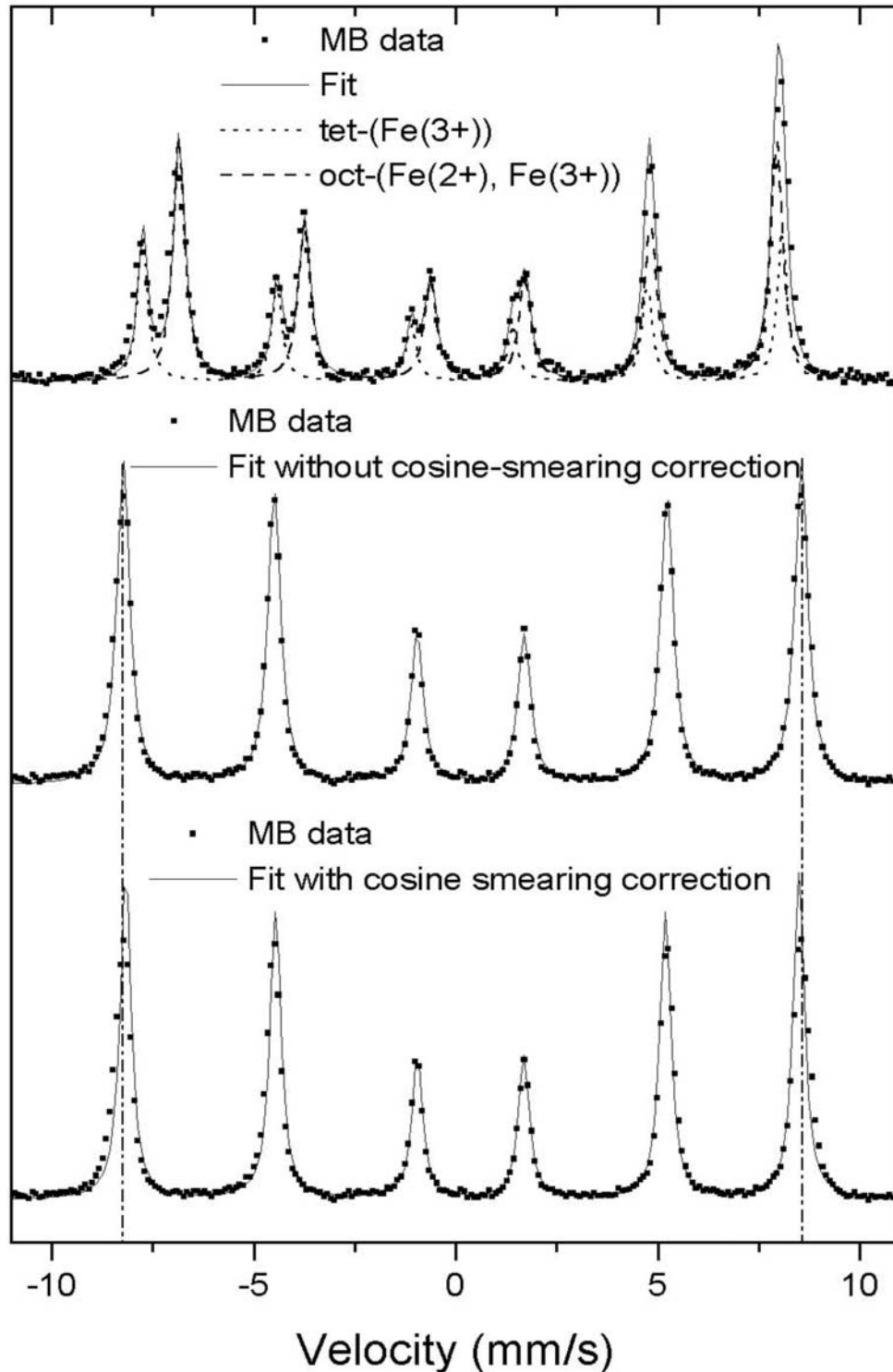
Figure 11. Mössbauer spectra (512 data channels folded to 256 channels) obtained at 293 K using an engineering-model MIMOS II spectrometer for rock slabs AREF043 and AREF121. The experiment time and source intensity for AREF043 were 49 hr and 25 mCi, which corresponds to a 12 hr integration at the Martian source intensity (∼100 mCi). The Mössbauer parameters derived from the fits indicate that the iron-bearing phases in AREF043 and AREF121 are magnetite and hematite, respectively. Spectrum AREF043 is magnetite with cosine smearing correction applied while fitting. Spectrum AREF121 of hematite shows the difference between a fit with and without correction for cosine smearing (red and green line respectively). See color version of this figure in the HTML.

information: (1) a PHA spectrum for each of the 5 detectors; (2) five Mössbauer spectra (one reference and four sample spectra) for each of the 13 temperature intervals for a total of 65 spectra; (3) reference and sample temperatures; and (4) engineering data (e.g., the error signal for the velocity transducer). The Mössbauer spectra are in counts per channel for 512 channels. In (2), the four sample Mössbauer spectra in each temperature interval can selected in a number of ways. For example, they can be the 14.4 keV spectrum from each of the four detectors or the sum of the 14.4 and 6.4 keV spectra for each of the four detectors. Alternatively, the four spectra can be 14.4 and 6.4 keV spectra, each summed over two detectors. The spectra can be analyzed individually or combined to produce higher quality spectra. Combining spectra from different temperature intervals will depend on how strongly the spectra depend on temperature.

[60] Spectral fitting routines (developed by our team) will be used to calculate Mössbauer parameters from the spectra. Normally, the velocity axis is calibrated using the spectra from the hematite plus α-Fe^0 reference absorber. The velocity locations of the peaks in the reference spectrum are accurately known through measurements as a function of temperature on Earth and measurement of the reference temperature during measurements on Mars. As a backup, the MIMOS II can also be calibrated against the magnetite CCT target. The fitting routines employ Lorentzian and other line shape functions and have integrated cosine smearing routines.

[61] For phase identification we will use our real-time database, which we have assembled from the literature and own measurements. This database consists of Mössbauer parameters (IS, QS, and B_{hf}), main site substitution, and behavior as a function of temperature for ~500 individual mineral phases. In addition, we also have Mössbauer spectra for over 1000 Martian analogue samples along with (incomplete) supporting chemical, magnetic, thermal emissivity, X-ray diffraction, and visible and near-IR spectral data. An implemented artificial neural network system was trained with our compiled database and will be used for quick mineral identification from measured Mössbauer parameters [de Souza, 1999; de Souza and Klingelhöfer, 2001]. Nevertheless, there are still many minerals for which relevant information, like f-factor dependence over composition and over the Martian temperature range, needs to be obtained through laboratory studies. We therefore are performing an extensive laboratory program to fill these
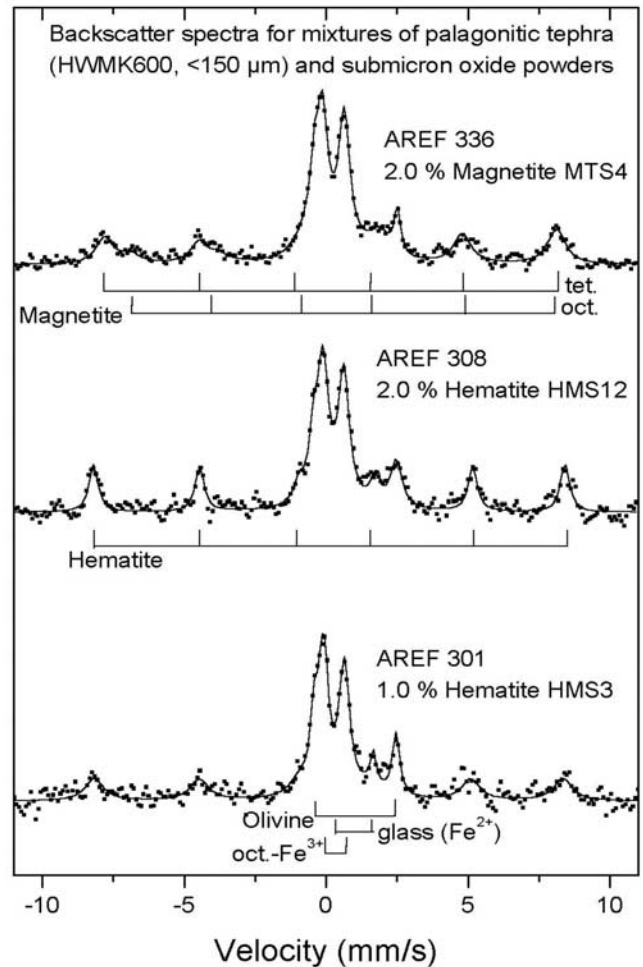

Figure 12. Mössbauer spectra (512 data channels folded to 256 channels) obtained at 293 K using an engineering-model MIMOS II spectrometer for mixtures of palagonitic tephra HWMK600 (<150 μm) and hematite HMS3 and HMS12 and magnetite MTS4. Experiment times were 10 h. See color version of this figure in the HTML.

gaps. Also, the temperature behavior of some compounds can be extrapolated on the basis of theoretical models. As we deal mostly with phases that contain Fe^{2+} and Fe^{3+}, the relative variation of f-factors between individual minerals in many cases is small, and for the data analysis we only need to have relative values normalized to one of the minerals present in the investigated sample.

References

Agresti, D. G., R. V. Morris, E. L. Wills, T. D. Shelfer, M. M. Pimperl, M. Shen, B. C. Clark, and B. D. Ramsey, Extraterrestrial Mössbauer spectrometry, *Hyperfine Interact.*, *72*, 285–298, 1992.

Aramu, F., and V. Maxia, Shift and broadening of Mössbauer peaks by lack of collimation, *Nucl. Instrum. Methods*, *80*, 35–39, 1970.

Table 1. Mössbauer Parameters for Spectra in Figure 11[a]

	IS, mm/s	QS, mm/s	B_{hf} T
Fits Using Lorentzian Line Shapes With Cosine Smearing Correction			
AREF043			
oct-(Fe^{2+}, Fe^{3+})	0.665(2)[a]	0.002(1)	45.8(1)
tet-Fe^{3+}	0.282(3)	−0.002(3)	49.0(1)
AREF121, oct-Fe^{3+}	0.377(1)	−0.198(1)	51.6(1)
Fits Using Pure Lorentzian Line Shapes			
AREF043			
oct-(Fe^{2+}, Fe^{3+})	0.666(1)	0.001(3)	46.1(1)
tet-Fe^{3+}	0.294(2)	0.012(4)	49.4(1)
AREF121, oct-Fe^{3+}	0.379(1)	−0.199(1)	52.0(1)

[a]The Mössbauer parameters are at 293 K. Numbers in parentheses are the statistical error only according to the chi-squared fit.

Arvidson, R. E., et al., Rocky 7 prototype Mars rover field geology experiments: 1. Lavic Lake and Sunshine Volcanic Field, California, *J. Geophys. Res.*, *103*, 22,671–22,688, 1998.

Arvidson, R. E., et al., Physical properties and localization investigations associated with the 2003 Mars Exploration rovers, *J. Geophys. Res.*, *108*(E12), 8070, doi:10.1029/2002JE002041, 2003.

Bancroft, G. M., *Mössbauer Spectroscopy: An Introduction for Inorganic Chemists and Geochemists*, McGraw-Hill, New York, 1973.

Bell, J. F., III, R. V. Morris, and J. B. Adams, Thermally altered palagonitic tephra: A spectral and process analog to the soil and dust of Mars, *J. Geophys. Res.*, *98*, 3373–3385, 1993.

Bell, J. F., III, et al., Mars Exploration Rover Athena Panoramic Camera (Pancam) investigation, *J. Geophys. Res.*, *108*(E12), 8063, doi:10.1029/2003JE002070, 2003.

Bishop, J. L., and E. Murad, Schwertmannite on Mars? Spectroscopic analyses of schwertmannite, its relationship to other ferric minerals, and its possible presence in the surface material on Mars, in *Mineral Spectroscopy: A Tribute to Roger G. Burns*, edited by M. D. Dyar, C. McCammon, and M. W. Schaefer, *Spec. Publ. Geochem. Soc.*, *5*, 337–358, 1996.

Bishop, J. L., C. M. Pieters, and R. G. Burns, Reflectance and Mössbauer spectroscopy of ferrihydrite-montmorillonite assemblages as Mars soil analog materials, *Geochim. Cosmochim. Acta*, *57*, 4583–4595, 1993.

Bishop, J. L., C. M. Pieters, R. G. Burns, J. O. Edwards, R. L. Mancinelli, and H. Froschel, Reflectance spectroscopy of ferric sulfate-bearing montmorillonites as Mars soil analogue materials, *Icarus*, *117*, 101–119, 1995.

Burns, R. G., Mössbauer spectral characterization of iron in planetary surface materials, in *Remote Geochemical Analysis: Elemental and Mineralogical Composition*, edited by C. M. Pieters and P. A. J. Englert, pp. 539–556, Cambridge Univ. Press, New York, 1993.

Burns, R. G., and D. S. Fisher, Iron-sulfur mineralogy of Mars: Magmatic evolution and chemical weathering products, *J. Geophys. Res.*, *95*, 14,415–14,421, 1990.

Burns, R. G., and S. L. Martinez, Mössbauer spectra of olivine-rich achondrites: Evidence for preterrestrial redox reactions, *Proc. Lunar Planet. Sci. Conf. 21st*, 331–340, 1991.

Burns, R. G., and T. C. Solberg, ^{57}Fe-bearing oxide, silicate, and aluminosilicate minerals: Crystal structure trends in Mössbauer spectra, in *Spectroscopic Characterization of Minerals and Their Surfaces*, pp. 262–283, Am. Chem. Soc., Washington, D. C., 1990.

Christensen, P. R., et al., Detection of crystalline hematite mineralization on Mars by the Thermal Emission Spectrometer, *J. Geophys. Res.*, *105*, 9623–9642, 2000.

Christensen, P. R., R. V. Morris, M. D. Lane, J. L. Bandfield, and M. C. Malin, Global mapping of Martian hematite mineral deposits: Remnants of water-driven processes on early Mars, *J. Geophys. Res.*, *106*, 23,873–23,885, 2001.

Christensen, P. R., et al., Miniature Thermal Emission Spectrometer for the Mars Exploration Rovers, *J. Geophys. Res.*, *108*(E12), 8064, doi:10.1029/2003JE002117, in press, 2003.

De Grave, E., and A. Van Alboom, Evaluation of ferrous and ferric Mössbauer fractions, *Phys. Chem. Miner.*, *18*, 337–342, 1991.

de Souza, P. A., Jr., Automation in Mössbauer spectroscopy analysis, *Lab. Robot. Automation*, *11*(1), 13–23, 1999.

de Souza, P. A., Jr., and G. Klingelhöfer, Mars-analogue minerals, soils, and rocks studied by Mössbauer spectroscopy, *Meteorit. Planet. Sci.*, *36A*, 139, 2001.

Evlanov, E. N., V. A. Frolov, O. F. Prilutski, A. M. Rodin, G. V. Veselova, and G. Klingelhöfer, Mössbauer spectrometer for mineralogical analysis of the Mars surface: Mössbauer source considerations, *Lunar Planet. Sci.*, 459–460, 1993.

Fegley, B., Jr., G. Klingelhöfer, R. A. Brackett, N. Izenberg, D. T. Kremser, and K. Lodders, Basalt oxidation and the formation of hematite on the surface of Venus, *Icarus*, *118*, 373–383, 1995.

Fernandez-Moran, H., S. S. Hafner, M. Ohtsuki, and D. Virgo, Mössbauer effect and high-voltage electron microscopy of pyroxenes in Type B samples, *Science*, *167*, 686–688, 1970.

Galazkha-Friedman, J., and J. Juchniewicz, Martian Mössbauer Spectrometer MarMös, project proposal, Space Res. Cent., Polish Acad. of Sci., Warsaw, Feb. 1989.

Gay, P., G. M. Bancroft, and M. G. Bown, Diffraction and Mössbauer studies of minerals from lunar soils and rocks, *Science*, *167*, 626–628, 1970.

Golden, D. C., R. V. Morris, H. V. Lauer Jr., and S. R. Yang, Mineralogy of three slightly palagonitized tephra samples from the summit of Mauna Kea, Hawaii, *J. Geophys. Res.*, *98*, 3401–3411, 1993.

Gonser, U., Mössbauer spectroscopy, in *Microscopic Methods in Metals*, edited by U. Gonser, chap. 13, pp. 409–448, Springer-Verlag, New York, 1986.

Gonser, U., F. Aubertin, S. Stenger, H. Fischer, G. Smirnov, and G. Klingelhöfer, Polarization and thickness effects in Mössbauer spectroscopy, *Hyperfine Interact.*, *67*, 701–710, 1991.

Gorevan, S., et al., Rock Abrasion Tool Mars Exploration Rover Mission, *J. Geophys. Res.*, *108*(E12), 8068, doi:10.1029/2003JE002061, in press, 2003.

Graff, T. G., R. V. Morris, and P. R. Christensen, Lunar mare basalts as analogues for Martian volcanic compositions: Evidence from visible, near-IR, and thermal emission spectroscopy, *Lunar Planet. Sci.* [CD-ROM], *XXXIV*, 1632, 2003.

Greenwood, N. N., and T. C. Gibb, *Mössbauer Spectroscopy*, Chapman and Hall, New York, 1971.

Gummer, A. W., Effect of accumulated decay product on the Mössbauer emission spectrum, *Nucl. Instrum. Methods Phys. Res., Sect. B*, *34*, 224–227, 1988.

Hargraves, R. B., D. W. Collinson, R. E. Arvidson, and P. M. Cates, Viking magnetic properties experiment: Extended mission results, *J. Geophys. Res.*, *84*, 8379–8384, 1979.

Hawthorne, F. C., Mössbauer spectroscopy, in *Spectroscopic Methods in Mineralogy and Geology, Rev. Mineral.*, vol. 18, edited by F. C. Hawthorne, pp. 255–340, Mineral. Soc. Am., Washington, D. C., 1988.

Held, P., PIN-Photodioden als Detektoren für das Mössbauerspektrometer MIMOS zur Untersuchung der Marsoberfläche, diploma thesis, Inst. for Nucl. Phys., Univ. Darmstadt, Darmstadt, Germany, 1993.

Held, P., MIMOS II: Ein miniaturisiertes Möβbauerspektrometer in Rückstreugeometrie zur mineralogischen Analyse der Marsoberfläche, Ph.D. thesis, Inst. for Nucl. Phys., Univ. Darmstadt, Darmstadt, Germany, 1997.

Held, P., R. Teucher, G. Klingelhöfer, J. Foh, H. Jäger, and E. Kankeleit, Mössbauer Spectrometer for mineralogical analysis of the Mars surface: First temperature dependent tests of the detector and drive system, *Lunar Planet. Sci.*, *XXIV*, 633–634, 1993.

Herkenhoff, K., et al., Athena Microscopic Imager investigation, *J. Geophys. Res.*, *108*(E12), 8065, doi:10.1029/2003JE002076, 2003.

Herzenberg, C. L., and D. L. Riley, Analysis of first returned lunar samples by Mössbauer spectrometry, *Proc. Lunar Sci. Conf. 1st*, 2221–2241, 1970.

Herzenberg, C. L., R. B. Moler, and D. L. Riley, Mossbauer instrumental analysis of Apollo 12 lunar rock and soil samples, *Proc. Lunar Sci. Conf. 2nd*, 2103–2123, 1971.

Housley, R. M., M. Blander, M. Abdel-Gawad, R. W. Grant, and A. H. Muir Jr., Mossbauer spectroscopy of Apollo 11 samples, *Proc. Lunar Sci. Conf. 1st*, 2251–2268, 1970.

Housley, R. M., R. W. Grant, A. H. Muir Jr., M. Blander, and M. Abdel-Gawad, Mossbauer studies of Apollo 12 samples, *Proc. Lunar Sci. Conf. 2nd*, 2125–2136, 1971.

Housley, R. M., E. H. Cirlin, and R. W. Grant, Characterization of fines from the Apollo 16 site, *Proc. Lunar Sci. Conf. 4th*, 2729–2735, 1973.

Huffman, G. P., F. C. Schwerer, and R. M. Fisher, Iron distributions and metallic-ferrous ratios for Apollo lunar samples: Mossbauer and magnetic analyses, *Proc. Lunar Sci. Conf. 5th*, 2779–2794, 1974.

Hviid, S. F., et al., Magnetic properties experiments on the Mars Pathfinder Lander: Preliminary results, *Science*, *278*, 1768–1770, 1997.

Johnson, G. R., and G. R. Olhoeft, Densities of rocks and minerals, in *CRC Handbook of Physical Properties of Rocks*, vol. III, edited by R. S. Carmichael, pp. 1–38, CRC Press, Boca Raton, Fla., 1984.

Kankeleit, E., Velocity spectrometer for Mössbauer experiments, *Rev. Sci. Instrum. 35*, 194–197, 1964.

Kankeleit, E., Some technical developments in Mössbauer spectroscopy, paper presented at International Conference on Mössbauer Spectroscopy, Univ. of Krakow, Krakow, Poland, 1975.

Klingelhöfer, G., The miniaturized spectrometer MIMOS II, in *Mössbauer Spectroscopy in Materials Science*, edited by M. Miglierini and D. Petridis, pp. 413–426, Kluwer Acad., Norwell, Mass., 1999.

Klingelhöfer, G., U. Imkeller, E. Kankeleit, and B. Stahl, Remarks on depth selective CEMS -backscattering measurements, *Hyperfine Interact.*, *71*, 1445–1448, 1992.

Klingelhöfer, G., B. Fegley Jr., R. V. Morris, E. Kankeleit, P. Held, and E. P. O. Evlanov, Mineralogical analysis of Martian soil and rock by a miniaturized backscattering Mössbauer spectrometer, *Planet. Space Sci.*, *44*, 1277–1288, 1996.

Klingelhöfer, G., P. Held, B. Bernhardt, J. Foh, R. Teucher, and E. Kankeleit, In-situ phase analysis by a versatile miniaturized Mössbauer spectrometer, *Hyperfine Interact.*, *111*, 331–334, 1998.

Knudsen, J. M., Mössbauer spectroscopy of ^{57}Fe and the evolution of the solar system, *Hyperfine Interact. 47*, 3–31, 1989.

Knudsen, J. M., S. Moerup, and J. Galazkha-Friedman, Mössbauer spectroscopy and the iron on Mars, *Hyperfine Interact.*, *57*, 2231–2234, 1990.

Knudsen, J. M., et al., Mössbauer spectroscopy on the surface of the planet Mars. Why?, *Hyperfine Interact.*, *68*, 83–94, 1992.

Lane, M. D., R. V. Morris, S. A. Mertzman, and P. R. Christensen, Evidence for platy hematite grains in Sinus Meridiani Mars, *J. Geophys. Res.*, *107*(E12), 5126, doi:10.1029/2001JE001832, 2002.

Madsen, M. B., S. Morup, T. V. V. Costa, J. M. Knudsen, and M. Olsen, Superparamagnetic component in the Orgueil meteorite and Mossbauer spectroscopy studies in applied magnetic fields, *Nature*, *29*, 501–503, 1986.

Madsen, M. B., S. F. Hviid, H. P. Gunnlaugsson, J. M. Knudsen, W. Goetz, C. T. Pedersen, A. R. Dinesen, C. T. Morgensen, M. Olsen, and R. B. Hargraves, The magnetic properties experiments on Mars Pathfinder, *J. Geophys. Res.*, *104*, 8761–8779, 1999.

Madsen, M., et al., Magnetic Properties Experiments on the Mars Exploration Rover mission, *J. Geophys. Res.*, *108*(E12), 8069, doi:10.1029/2002JE002029, in press, 2003.

Maki, J. N., et al., Mars Exploration Rover engineering cameras, *J. Geophys. Res.*, *108*(E12), 8071, doi:10.1029/2003JE002077, in press, 2003.

McCammon, C., Mössbauer spectroscopy of minerals, in *Mineral Physics and Crystallography: A Handbook of Physical Constants*, AGU Ref. Shelf, vol. 2, edited by T. J. Ahrens, pp. 332–347, AGU, Washington, D. C., 1995.

Morris, R. V., H. V. Lauer Jr., C. A. Lawson, E. K. Gibson Jr., G. A. Nace, and C. Stewart, Spectral and other physicochemical properties of submicron powders of hematite (α-Fe$_2$O$_3$), maghemite (γ-Fe$_2$O$_3$), magnetite (Fe$_3$O$_4$), goethite (α-FeOOH), and lepidocrocite (γ-FeOOH), *J. Geophys. Res.*, *90*, 3126–3144, 1985.

Morris, R. V., D. G. Agresti, T. D. Shelfer, and T. J. Wdowiak, Mössbauer spectroscopy for mineralogical analysis on planetary surfaces, paper presented at SAAP Instrument Technology Workshop, Sample Acquisition and Anal. Program, Houston, Tex., 14–16 Nov. 1988.

Morris, R. V., D. G. Agresti, H. V. Lauer Jr., J. A. Newcomb, T. D. Shelfer, and A. V. Murali, Evidence for pigmentary hematite on Mars based on optical magnetic and Mössbauer studies of superparamagnetic (nanocrystalline) hematite, *J. Geophys. Res.*, *94*, 2760–2778, 1989.

Morris, R. V., J. J. Gooding, H. V. Lauer Jr., and R. B. Singer, Origins of Marslike spectral and magnetic properties of a Hawaiian palagonitic soil, *J. Geophys. Res.*, *95*, 14,427–14,434, 1990.

Morris, R. V., D. C. Golden, J. F. Bell III, H. V. Lauer Jr., and J. B. Adams, Pigmenting agents in Martian soils: Inferences from spectral, Mössbauer, and magnetic properties of nanophase and other iron oxides in Hawaiian palagonitic soil PN-9, *Geochim. Cosmochim. Acta*, *57*, 4597–4609, 1993.

Morris, R. V., D. C. Golden, J. F. Bell III, and H. V. Lauer Jr., Hematite, pyroxene, and phyllosilicates on Mars: Implications from oxidized impact melt rocks from Manicouagan Crater Quebec, Canada, *J. Geophys. Res.*, *100*, 5319–5328, 1995.

Morris, R. V., D. W. Ming, D. C. Golden, and J. F. Bell III, An occurrence of jarositic tephra on Mauna Kea, Hawaii: Implications for the ferric mineralogy of the Martian surface, in *Mineral Spectroscopy: A Tribute to Roger G. Burns*, edited by M. D. Dyar, C. McCammon, and M. W. Schaefer, *Spec. Publ. Geochem. Soc.*, *5*, 327–336, 1996.

Morris, R. V., D. C. Golden, and J. F. Bell III, Low-temperature reflectivity spectra of red hematite and the color of Mars, *J. Geophys. Res.*, *102*, 9125–9133, 1997.

Morris, R. V., G. Klingelhöfer, R. L. Korotev, and T. D. Shelfer, Mössbauer mineralogy on the Moon: The lunar regolith, *Hyperfine Interact.*, *117*, 405–432, 1998a.

Morris, R. V., S. W. Squyres, J. F. Bell III, T. Economou, G. Klingelhoefer, P. Held, L. A. Haskin, A. Wang, B. L. Jolliff, and R. Rieder, Analysis of Martian surface materials during the Mars Surveyor 001 mission by the Athena instrument payload (abstract), *Lunar Planet. Sci.* [CD-ROM], *XXIX*, abstract 1326, 1998b.

Morris, R. V., et al., Mineralogy, composition, and alteration of Mars Pathfinder rocks and soils: Evidence from multispectral, elemental, and magnetic data on terrestrial analogue, SNC meteorite, and Pathfinder samples, *J. Geophys. Res.*, *105*, 1757–1817, 2000.

Morris, R. V., D. C. Golden, D. W. Ming, T. D. Shelfer, L. C. Jorgensen, J. F. Bell III, T. G. Graff, and S. A. Mertzman, Phyllosilicate-poor pala-gonitic dust from Mauna Kea Volcano (Hawaii): A mineralogical analogue for magnetic Martian dust?, *J. Geophys. Res.*, *106*, 5057–5083, 2001a.

Morris, R. V., T. G. Graff, T. D. Shelfer, and J. F. Bell III, Effect of palagonitic dust coatings on visible, near-IR and Mössbauer spectra of rocks and minerals: Implications for mineralogical remote sensing of Mars (abstract), *Lunar Planet. Sci.* [CD-ROM], *XXXII*, abstract 1912, 2001b.

Prilutskii, O., Internal report from Minsk, Space Res. Inst. (IKI), Moscow, 1990.

Rieder, R., R. Gellert, J. Brückner, G. Klingelhöfer, G. Dreibus, A. Yen, and S.W. Squyres, The new Athena alpha particle X-ray spectrometer for the Mars Exploration Rovers, *J. Geophys. Res.*, *108*(E12), 8066, doi:10.1029/2003JE002150, 2003.

Riesenman, R., J. Steger, and E. Kostiner, Cosine effect in Mössbauer spectroscopy involving a source of non-zero radius, *Nucl. Instrum. Methods*, *72*, 109–110, 1969.

Schröder, C., Optimierung der Nachweiseigenschaften des miniaturisierten Mössbauer-Spektrometers MIMOS II und Messungen an Mars-Analog-Proben, diploma thesis, Johannes Gutenberg Univ., Mainz, Germany, 2001.

Sims, M. R., et al., Performance characteristics of the PAW instrumentation on Beagle 2 (the astrobiology lander on ESA's Mars Express Mission), *Proc. SPIE Int. Soc. Opt. Eng.*, *4859*, 32–44, 2002.

Solberg, T. C., and R. G. Burns, Iron Mossbauer spectral study of weathered Antarctic and SNC meteorites, *Proc. Lunar Planet. Sci. Conf., 19th*, 313–322, 1989.

Squyres, S. W., et al., Athena Mars Rover science investigation, *J. Geophys. Res.*, *108*(E12), 8062, doi:10.1029/2003JE002121, in press, 2003.

Stevens, J. G., A. M. Khasanov, J. W. Miller, H. Pollak, and Z. Li (Eds.), *Mössbauer Mineral Handbook*, 527 pp., Biltmore, Ashville, N. C., 1998.

Straub, D. W., R. G. Burns, and S. F. Pratt, Spectral signature of oxidized pyroxenes: Implications to remote sensing of terrestrial planets, *J. Geophys. Res.*, *96*, 18,819–18,830, 1991.

Teucher, R., Miniaturisierter Mössbauerantrieb, diploma thesis, Inst. for Nucl. Phys., Univ. Darmstadt, Darmstadt, Germany, 1994.

Vieira, V. W. A., T. V. V. Costa, H. G. Jensen, J. M. Knudsen, and M. Olsen, Oxidation state of iron in SNC meteorites as studied by Mössbauer spectroscopy, *Phys. Scr.*, *33*, 180–186, 1986.

Wade, M. L., D. G. Agresti, T. J. Wdowiak, and L. P. Armendarez, A Mössbauer investigation of iron-rich terrestrial hydrothermal vent systems: Lessons for Mars exploration, *J. Geophys. Res.*, *104*, 8489–8507, 1999.

Wdowiak, T. J., and D. G. Agresti, Presence of a superparamagnetic component in the Orgueil meteorite, *Nature*, *311*, 140–142, 1984.

Wegener, H., *Der Mössbauer-Effect und Seine Anwendungen in Physik und Chemie*, 2nd ed., Bibliogr. Inst., Mannheim, Germany, 1966.

Weinheimer, C., M. Schrader, J. Bonn, T. Loeken, and H. Backe, Measurement of energy resolution and dead layer thickness of LN2-cooled PIN photodiodes, *Nucl. Instrum. Methods, Sect. A*, *311*, 273–279, 1992.

Wertheim, G. K., *Mössbauer Effect: Principles and Applications*, Academic, San Diego, Calif., 1964.

B. Bernhardt, P. A. de Souza Jr., J. Foh, R. Gellert, G. Klingelhöfer, D. Rodionov, and C. Schröder, Fachbereich Chemie und Pharmazie, Institut für Anorganische und Analytische Chemie, Johannes Gutenberg-Universität Mainz, Staudinger Weg 9, D-55099 Mainz, Germany. (klingel@mail.uni-mainz.de)

U. Bonnes and E. Kankeleit, Nuclear Physics Institute, Darmstadt University of Technology, 64289 Darmstadt, Germany.

E. Evlanov, S. Linkin, O. Prilutski, and B. Zubkov, Space Research Institute IKI, Moscow, Russia.

R. V. Morris, NASA Johnson Space Center, Mail Code SN3, Houston, TX 77058, USA.

S. W. Squyres, Department of Astronomy, Cornell University, 428 Space Sciences Building, Ithaca, NY 14853, USA.